



저작자표시-비영리-변경금지 2.0 대한민국

이용자는 아래의 조건을 따르는 경우에 한하여 자유롭게

- 이 저작물을 복제, 배포, 전송, 전시, 공연 및 방송할 수 있습니다.

다음과 같은 조건을 따라야 합니다:



저작자표시. 귀하는 원저작자를 표시하여야 합니다.



비영리. 귀하는 이 저작물을 영리 목적으로 이용할 수 없습니다.



변경금지. 귀하는 이 저작물을 개작, 변형 또는 가공할 수 없습니다.

- 귀하는, 이 저작물의 재이용이나 배포의 경우, 이 저작물에 적용된 이용허락조건을 명확하게 나타내어야 합니다.
- 저작권자로부터 별도의 허가를 받으면 이러한 조건들은 적용되지 않습니다.

저작권법에 따른 이용자의 권리는 위의 내용에 의하여 영향을 받지 않습니다.

이것은 [이용허락규약\(Legal Code\)](#)을 이해하기 쉽게 요약한 것입니다.

[Disclaimer](#)

공학박사 학위논문

**Multiscale poroacoustic modelling of
fibrous acoustical materials using
artificial intelligence**

인공지능을 이용한 섬유형 음향재료의
다중 스케일 음향 모델 연구

2021년 8월

서울대학교 대학원

기계항공공학부

전 주 현

**Multiscale poroacoustic modelling of fibrous
acoustical materials using artificial intelligence**

인공지능을 이용한 섬유형 음향재료의

다중 스케일 음향 모델 연구

지도교수 강 연 준

이 논문을 공학박사 학위논문으로 제출함

2021년 4월

서울대학교 대학원

기계항공공학부

전 주 현

전주현의 공학박사 학위논문을 인준함

2021년 6월

위 원 장 _____

부위원장 _____

위 원 _____

위 원 _____

위 원 _____

ABSTRACT

Multiscale poroacoustic modelling of fibrous acoustical materials using artificial intelligence

Ju Hyun Jeon

School of Mechanical and Aerospace Engineering

The Graduate School

Seoul National University

This study proposes a methods for estimating the intrinsic parameters and sound absorption coefficient of single or multi-layered fibrous materials using artificial intelligence. In the first phase of this work, convolutional neural network models (CNNs) for estimating intrinsic parameters of a single fibrous layer from X-ray micro-computed tomography (CT) images are introduced. Two-dimensional micro-CT images and numerically obtained intrinsic parameters were used to train the CNNs; Stokes flow and potential flow were used to numerically obtain the intrinsic parameters using geometrical models extracted from

the raw CT images. Then analogously to constructing a 3-D image of the fibrous material by stacking the 2-D slice images, the volumetric intrinsic parameters of the fibrous materials were calculated using the parameters of each 2-D image predicted by the trained CNN models. The intrinsic parameters of the fibrous volume predicted by the CNN models showed good agreement with the measured values. In addition, the sound absorption coefficient was calculated by applying both the predicted and measured intrinsic parameters to the semi-phenomenological sound propagation model and compared with the measured sound absorption coefficient. The results of the study confirm the feasibility of predicting intrinsic parameters of fibrous materials using a neural network model based on raw micro-CT images. In the second phase of this work, The feasibility of an artificial neural network (ANN) for the estimation of the sound absorption coefficient of a layered fibrous material is studied. The sound absorption coefficient of a four-layered fibrous material was estimated using a well-trained ANN model with only one intrinsic parameter: the static airflow resistivity (σ). The results indicated that the ANN model exhibits a good correlation between the estimated and measured absorption coefficient. The training data sets were built by carrying out experimental measurements using a two-microphone

impedance measurement tube with 230 combinations of four-layered fibrous materials. The results of the ANN are compared in three different cases with the transfer matrix method (TMM), which is the conventional method of estimating the sound absorption coefficient of multi-layers using several intrinsic parameters. The sound propagation model in acoustical material for the TMM was used by two models proposed by Delany-Bazely and Johnson-Champoux-Allard. By comparing the estimated sound absorption coefficient from the ANN and TMM with measured values, it was demonstrated that the model developed in this work gives more accurate results within the defined conditions. The results were compared in the frequency range of 3000-6000 Hz, and the error of the ANN model was less than 1.67 %.

Keywords: Artificial intelligence, Convolutional neural network, Intrinsic parameter, Micro-computed tomography, Numerical analysis, Sound absorption coefficient, Fibrous material, Multi-layered porous media

Student Number: 2013-23086

TABLE OF CONTENTS

ABSTRACT	i
LIST OF TABLES.....	vi
LIST OF FIGURES.....	vii
I. INTRODUCTION	1
II. PHYSICAL CHARACTERIZATION OF FIBROUS	
MATERIAL.....	8
2.1 Introduction	8
2.2 Microscopic geometrical characterization.....	9
2.2.1 X-ray micro-computerized tomography imaging.....	9
2.2.2 Two-dimensional geometrical model for fibrous material	11
III. EXPERIMENTAL PROCEDURES.....	16
3.1 Introduction	16
3.2 Numerical experiments for obtaining intrinsic parameters	17
3.2.1 Model for porosity and thermal characteristic length.....	17
3.2.2 Model for tortuosity and viscous characteristic length.....	18
3.2.3 Model for static airflow resistivity	23
3.3 Intrinsic parameter measurement	25
3.4 Sound absorption coefficient measurement.....	27
IV. NEURAL NETWORK MODEL DEVELOPMENT FOR	
INTRINSIC PARAMETERS OF FIBROUS MATERIAL.....	35
4.1 Introduction	35

4.2 Artificial neural network	36
4.2.1 Fully-connected artificial neural network	36
4.2.2 Convolutional neural network	41
4.3 Materials and model development	43
4.4 Model validation	47
4.5 Limitations of the model	53
V. NEURAL NETWORK MODEL DEVELOPMENT FOR	
MULTI-LAYERED FIBROUS MATERIAL	82
5.1 Introduction	82
5.2 Materials and model development	83
5.3 Conventional acoustical impedance models.....	86
5.3.1 Transfer matrix for layered fibrous material	86
5.3.2 Empirical model and motionless skeleton model.....	88
5.4 Model validation	92
5.4.1 Case no.1	94
5.4.2 Case no.2	95
5.4.3 Case no.3	96
5.5 Limitation of the model.....	98
VI. CONCLUSION	115
REFERENCES.....	118
국 문 초 록.....	126

LIST OF TABLES

Table 3.1 Measured intrinsic parameters of the three testing PET specimens.	29
Table 4.1 Detailed layer information of the developed CNN model architecture.	57
Table 4.2 Errors between the 3-D and 2-D numerical analysis of the reconstructed fiber models according to the orientation angles....	58
Table 4.3 Intrinsic parameters predicted using CNNs of the three samples of each testing PET and error from the mean of measured value.	59
Table 4.4 Comparison of the estimated intrinsic parameters and solving time between the 3-D numerical analysis and CNN model analysis for testing PETs.	60
Table 4.5 Detailed information on micro-CT image acquisition, modelling, and computation time.....	61
Table 4.6 Error of the intrinsic parameters obtained using 2-D slice geometries of the single fiber strand model.	62
Table 4.7 The static thermal permeability of testing PETs obtained using 3-D heat transfer analysis.....	63
Table 5.1 Properties of PET and RESIN felts.	99
Table 5.2 Intrinsic parameters of PET and RESIN felts.....	100

LIST OF FIGURES

Figure 2.1 (a) Isometric view, (b) top view, and (c) side vie of the 600 GSM PET felt. The gray square of the Fig. 2.1(a) coincides with the plane of micro-CT image plane.	13
Figure 2.2 (a) Micro-CT raw image of PET felt, (b) binary threshold image, and (c) active points clustered using DB-SCAN.....	14
Figure 2.3 (a) Cluster centroid connections, (b) reconstruction of the 2-D geometrical model from the 3-D fiber model, and (c) overlaid image of the 2-D geometrical model and micro-CT image.....	15
Figure 3.1 2-D mesh model constructed using the geometrical model. The square box in the figure is an area for visual reference of potential flow analysis to obtain tortuosity and VCL in Fig. 3.2 and Fig. 3.3.	30
Figure 3.2 Streamlines of inviscid flow formed in the square box in Fig. 3.1.	31
Figure 3.3 Velocity field of inviscid flow formed in the square box in Fig. 3.1.	32
Figure 3.4 Analyzed pressure field from the 2-D geometrical model using stokes flow.....	33
Figure 3.5 Schematic of the two-microphone impedance measurement tube (B & K Type 4206).....	34
Figure 4.1 Schematic architecture of a typical feedforward neural network.	64

Figure 4.2 Detailed structure of an artificial neuron.	65
Figure 4.3 6-layer (3-convolutional layer, 3-fully connected layer) architecture of the CNN model for AFR.	66
Figure 4.4 The trend of prediction error of static airflow resistivity according to the number of training datasets.	67
Figure 4.5 (a) Porosity and (b) summation of the line integration of the corrected fiber perimeter of 1500 testing images predicted using each CNN model and the values obtained using numerical analysis.	68
Figure 4.6 (a) Summation of the line integration of the squared velocity over the fiber skin and (b) summation of the area integration of the squared velocity in the pore of 1500 testing images predicted using each CNN model and the values obtained using numerical analysis.	69
Figure 4.7 (a) Tortuosity and (b) static airflow resistivity of 1500 testing images predicted using each CNN model and the values obtained using numerical analysis.	70
Figure 4.8 The intrinsic parameters predicted using CNNs corresponding to each slice image constituting the fibrous volume.	71
Figure 4.9 Change of intrinsic parameter values according to x-axis image resolution; (a) porosity, (b) tortuosity and (c) static airflow resistivity.	72
Figure 4.10 Change of intrinsic parameter values according to x-axis image resolution; (a) TCL and (b) VCL.	73

Figure 4.11 Comparison of measured and predicted intrinsic parameters; (a) porosity, (b) tortuosity.	74
Figure 4.12 Comparison of measured and predicted intrinsic parameters; (a) static airflow resistivity, (b) thermal characteristic length.	75
Figure 4.13 Comparison of measured and predicted intrinsic parameters; viscous characteristic length.....	76
Figure 4.14 (a) 3-D geometrical for testing PET B #1 (b) streamlines obtained from potential flow analysis, (c) pressure field obtained from Stokes flow analysis.....	77
Figure 4.15 Normal incidence sound absorption coefficient of the PET A.	78
Figure 4.16 Normal incidence sound absorption coefficient of the PET B.	79
Figure 4.17 Normal incidence sound absorption coefficient of the PET C.	80
Figure 4.16 Heat diffusion field (\mathbf{u}) [$\times 10^{-10}\text{m}^2$] of the testing PETs. (a) PET A #3, (b) PET B #1 and (c) PET C #2.	81
Figure 5.1 Example of a four-layered PET sample with a circular cross-section.	101
Figure 5.2 26 four-layered fibrous felt samples used in Case no.1.	102
Figure 5.3 26 four-layered fibrous felt samples used in Case no.2.	103

Figure 5.4 26 four-layered fibrous felt samples used in Case no.3.	104
Figure 5.5 Structure of the ANN developed for estimating the sound absorption coefficient of a layered fibrous material.....	105
Figure 5.6 Trend of loss (percentage error) versus the number of training iterations (epochs).	106
Figure 5.7 MAPE of estimated sound absorption coefficient using the TMM-DB (△), TMM-JCA (○), and ANN model (×) for Case 1.	107
Figure 5.8 Estimated sound absorption coefficient using an ANN for one randomly selected sample out of 26 samples for Case 1. (sample 10 in Fig. 5.2).....	108
Figure 5.9 Estimated sound absorption coefficient of 26 samples at 4000 Hz using (a) TMM-DB, (b) TMM-JCA, and (c) ANN model for Case 1.	108
Figure 5.10 MAPE of estimated sound absorption coefficient using the TMM-DB (△), TMM-JCA (○), and ANN model (×) for Case 2.	109
Figure 5.11 Estimated sound absorption coefficient using an ANN for Case 2, wherein the sample consisted of four layers of new PET. (sample 18 in Fig 5.3).....	110
Figure 5.12 Estimated sound absorption coefficient of 26 samples at 4000 Hz using (a) TMM-DB, (b) TMM-JCA, and (c) ANN model for Case 2.	110
Figure 5.13 MAPE of estimated sound absorption coefficient using the TMM-	

DB (Δ), TMM-JCA (\bigcirc), and ANN model (\times) for Case 3.	111
Figure 5.14 Estimated sound absorption coefficient using an ANN for Case 3, wherein the sample consisted of four layers of RESIN. (sample 18 in Fig 5.4)	112
Figure 5.15 Micro computed tomography images of (a) PET and (b) RESIN felt. (2800 \times 2800 \times 1950 voxels with a resolution of 0.95 $\mu\text{m}/\text{voxel}$)	113
Figure 5.16 Estimated sound absorption coefficient of 26 samples at 4000 Hz using (a) TMM-DB, (b) TMM-JCA, and (c) ANN model for Case 3.	114

CHAPTER 1

INTRODUCTION

Fibrous materials are porous materials that are widely used for noise control. Generally, these materials are applied to the surface of a space to block external noise or to control the sound absorption coefficient of the space. Specifically, fibrous materials are used to control the interior sound pressure levels of vehicles such as automobiles, trains, and airplanes. However, to control the indoor noise level of a mechanical system using acoustical materials, it is necessary to understand the precise performance measures of the materials. [1, 2]

In general, models used to describe the acoustic properties of fibrous materials can be categorized as empirical models and semi-phenomenological (motionless skeleton) models. The model proposed by Delaney and Bazely is representative of empirical models. [3] The model uses a single intrinsic parameter, static airflow resistivity, to predict the acoustic properties of fibrous materials. Numerous empirical formulas have been proposed to improve the model accuracy or to predict the acoustic performance of various materials. [4, 5] Empirical models are widely used because of their convenience; however,

their performance may decrease depending on the material. [6] Semi-phenomenological models have been developed to overcome this limitation of application to various materials. Johnson et al. proposed a model that expresses the complex bulk density of air in acoustical materials, which describes the effect of viscous resistance. [7] Champoux and Allard proposed a model that expresses the complex bulk modulus of air in acoustical materials, which describes the effect of thermal conduction in the material. [8] These two models can be applied to an arbitrary pore shape inside the porous media. The complex bulk density and complex bulk modulus obtained from the two models have been applied to the cylindrical tube model proposed by Zwikker and Kosten [9] to predict the acoustic properties of porous media. This is commonly referred to as the Johnson-Champoux-Allard (JCA) model, which requires knowledge of five intrinsic parameters: porosity, tortuosity, static airflow resistivity, viscous characteristic length (VCL), and thermal characteristic length (TCL). Subsequently, Lafarge et al. and Pride et al. modified the JCA model to improve prediction accuracy at low frequencies. [10, 11] In the model presented by Lafarge et al., [10] static thermal permeability is included in addition to the five parameters required in the JCA model. In the case of the model suggested by Pride et al., [11] static thermal permeability, static viscous tortuosity, and static thermal tortuosity are included in addition to the five parameters.

Because it is difficult to guarantee the accuracy of empirical models for various materials, the JCA, JCA-Lafarge, and JCA-Pride-Lafarge models are generally used to predict the acoustic performance of fibrous materials. The three models consider only airborne noise in porous media and assume that the skeleton of the material is motionless. Therefore, all intrinsic parameters required to construct the models represent the fluid characteristics inside the porous media. Conventionally, the five parameters required in the JCA model can be obtained using well-organized measurement methods, [12, 13, 14, 15, 16] but the measurement process is labor intensive and requires proficiency in the use of the measuring instruments. To overcome these disadvantages, numerous studies have been conducted to predict the intrinsic parameters of materials. In particular, studies on predicting intrinsic parameters through numerical analysis using the geometrical information of porous media microstructures have been conducted for decades. Tarnow proposed an explicit equation to express the static airflow resistivity of a fibrous material by randomly arranging the cross-sections of fibers with a single radius on a two-dimensional (2-D) plane using Voronoi polygons. [17, 18] The static airflow resistivity of the material was calculated using Stokes flow analysis in the lateral direction of the randomly arranged fibers. Subsequently, Hirose and Nakagawa proposed a method for obtaining all five intrinsic parameters using

Stokes flow analysis and potential flow analysis based on 200 strands of fibers randomly arranged in a 2-D plane. [19] As research on microstructures of porous media in three-dimensions (3-D), studies on open-cell foam have been actively conducted. Perrot et al. proposed periodic unit cells for open-cell foam to predict intrinsic parameters through numerical analysis. [20, 21, 22] Park et al. introduced a method for optimizing the sound absorption of polyurethane foam using periodic unit cell analysis. [23, 24] Finally, Luu et al. proposed a method to obtain intrinsic parameters through a fiber reconstruction technique based on scanning electron microscope (SEM) imaging, contributing to the research on the 3-D microstructure of fibrous material. [25, 26] These methods have a common goal of constructing geometrical information from the microstructure of porous media and using it to predict intrinsic parameters through numerical analysis. With another approach, Lieblappen et al. considered snow as a natural porous medium, and predicted the porosity and tortuosity of the porous medium using micro-computerized tomography (CT) imaging and ultrasonic waves. [27] Lee et al. proposed semi-phenomenological and empirical models that relate the microstructural properties to the intrinsic parameters using micro-CT imaging. [28] However, because these models were developed using polyurethane foam, they cannot predict the intrinsic parameters of fibrous materials.

In first phase of this work, to build upon these previous studies, I propose a method to predict intrinsic parameters of fibrous materials using artificial intelligence. The five basic intrinsic parameters required by the JCA model are covered in this work. Previously, Lähivaara proposed a methodology, using a deep convolutional neural network (CNN), that estimates the porosity and tortuosity of materials based on the wave field pattern inside porous media using ultrasound. [29] In this work, I take an approach from easily obtainable image information. 3-D X-ray micro-CT imaging was used to obtain geometrical information of the microstructure of real fibrous materials; 3-D CT imaging allows the reconstruction of the volume render image by stacking multiple 2-D slice images. Based on this concept, the microstructural geometry of the fibers was extracted for each CT slice image, and numerical analysis was conducted in 2-D to predict the intrinsic parameters for each slice image. I employed the finite element method for a steady incompressible Stokes flow to obtain the static airflow resistivity [30, 31] and the boundary element method for a potential flow to obtain the tortuosity and VCL. [32, 33, 34] Porosity and TCL were obtained directly from the fiber geometry. The slice images of a fibrous material can be stacked to reconstruct the volume structure, and then the intrinsic parameters of the volume can be calculated using the value of each fiber geometry slice. In this process, the effects of the fluid flow in the direction

normal to the 2-D image plane are ignored. In addition, CNNs [35, 36] were employed to 2-D micro-CT raw images. The CNN models for each intrinsic parameter were trained based on a large dataset of raw slice CT images and the intrinsic parameters obtained from numerical analysis. The intrinsic parameter values obtained using the trained CNNs were compared with parameter values obtained from 3-D model analysis and measured at the macro scale using conventional measurement methods to validate the proposed method.

In second phase of this work, the method of predicting the absorption coefficient of multi-layered fibrous materials using the fully-connected artificial neural network (ANN) is discussed. The objective of the work in second phase is to accurately estimate the sound absorption coefficient of multi-layered fibrous material by using only one intrinsic parameter as an input variable. The neural network model developed in the second phase, uses one intrinsic parameter (static airflow resistivity) and shows better estimation accuracy than the conventional transfer matrix method (TMM) [37, 38, 39] using one or five parameters.

This paper is organized as follows. First, chapter 2 explains the process of constructing geometrical information of the fibrous materials using the micro-CT images. Then, chapter 3 presents the process of constructing a numerical model and obtaining five intrinsic parameters using 2-D micro-CT images.

Next, chapter 4 presents the CNN models and the data structures used to train the model. After comparing predicted and measured values, the results and verifications are presented. Chapter 5 explains the ANN model used to estimating the acoustical property of multi-layered fibrous material. Then the estimated sound absorption coefficient using ANN and TMM is compared with measured values. Finally, the conclusions are discussed in Sec. VI.

CHAPTER 2

PHYSICAL CHARACTERIZATION OF FIBROUS MATERIAL

2.1 Introduction

In this chapter, the process for constructing a 2-D geometrical model is described using X-ray micro-CT image of fibrous material. In order to accurately analyze the flow field in the fibrous material, it is important to find the optimal condition considering the effect of resolution and size of the micro-CT image. In this work, the density-based spatial clustering of applications with noise (DB-SCAN) algorithm was used to extract information such as the centroid, perimeter, and diameter of fiber strands distributed on the micro-CT images. Polyethylene terephthalate was used in this work for the basic material, which is widely used for sound insulation in the interior of the automotive vehicle.

2.2 Microscopic geometrical characterization

2.2.1 X-ray micro-computerized tomography imaging

Nine polyethylene terephthalate (PET) felts with a thickness of approximately 10 mm and a surface density from 600 to 1400 grams per square meter (GSM) at intervals of 100 GSM were used in this work. Six of these specimens were used to generate a dataset to train the CNNs, and the other three specimens were used to test the performance of the trained CNNs. Tomography was conducted on nine types of PET using an X-ray micro-imaging system (Skyscan 1172, Bruker, Belgium). For micro-CT imaging, each specimen was prepared 20 mm long in a 4 mm \times 4 mm cross-section. The voltage and current of the X-ray source were set to 40 kV and 250 μ A, respectively, and the exposure time was set to 2356 ms.

A previous microstructure study on fibrous material [25] confirmed that the standard deviation of the intrinsic parameters calculated according to a random position in the fibrous material is very small when the cubic box dimension of the micro volume is 1000 μ m or more. Using this point, I set the 3-D image size to be analyzed as 1000 \times 1000 \times 1000 μ m³. The resolution of the image was set to 2 μ m/voxel, thus using an image of 500 \times 500 \times 500 voxels.

The resolution of the image was determined considering both the computational cost and accuracy of the analysis. Because the diameter of fibers constituting the PET fibrous material used in this study was mostly between 20 and 60 μm , and the pore size was much larger than this, a resolution of 2 μm was considered suitable for analysis. [40] The slice images were stacked to reconstruct a 3-D image using cone-beam reconstruction software (NRecon, Brucker, Belgium). For visual reference, a part of the 3-D geometrical model of 600 GSM PET is shown in Fig. 2.1. Micro-CT images were taken on the y-z plane of the fibrous volume. Therefore, 2-D images can be analyzed in the y and z direction. The 2-D flow analysis covered in chapter III considers the z-direction flow, and the 3-D flow analysis which will be covered in chapter IV, also considers the flow in the z-direction.

2.2.2 Two-dimensional geometrical model for fibrous material

This section describes the algorithm used to reconstruct a 2-D geometrical model of felt fibers based on 3-D micro-CT images. The algorithm uses a DB-SCAN [41] to identify illuminated pixels in micro-CT images and group them into clusters representing the section of a fiber on the image plane. The process of extracting the 2-D geometrical model from the micro-CT slice image is shown in Fig. 2.2 and Fig. 2.3. For clarity, this section uses a 3-D image of $480 \times 480 \times 200 \mu\text{m}^3$.

First, from the raw image shown in Fig. 2.2(a), the pores and fibers are distinguished using a binary threshold, as shown in Fig. 2.2(b). The pixels included in the region of the fiber are designated active pixels. The coordinates of the active pixels in each slice image are extracted from the image file at this stage. The active point coordinates are then clustered using DB-SCAN, as shown in Fig. 2.2(c). Cluster objects were created by extracting the cluster centroid, cluster tag, cluster point coordinates, and the number of points in the cluster. Cluster objects were then used to deduce the boundary ellipse containing the respective clusters. Note that, as shown by the arrows in Fig. 2.2(b) and Fig. 2.2(c), a single micro-CT image may fail to separate a plurality of adjacent fibers. To overcome this problem, cluster objects in the images

immediately before and after the image of interest were examined to determine whether the cluster consisted of one fiber or a plurality of fibers.

The center of each fiber detected in the slice image can be presented in three-axis coordinates, as shown in Fig. 2.3(a). To create a continuous cylinder along this centerline, the diameter of the cylinder was taken to be the average length of the minor axis of the ellipse deduced from the cluster of each slice image. The diameter of the fibers of PET felt used in this study follows the normal distribution with an average of $29\text{ }\mu\text{m}$ and a standard deviation of $10\text{ }\mu\text{m}$. Here, it is assumed that the diameter of a single fiber is constant in the centerline direction. In the 3-D fiber geometrical model shown in Fig. 2.3(b), it is possible to obtain a 2-D geometrical model for an arbitrary position in the x-axis direction. The 2-D geometrical model reconstructed from the x-axis position of the raw image shown in Fig. 2.2(a) is overlaid with the raw image in Fig. 2.3(c).

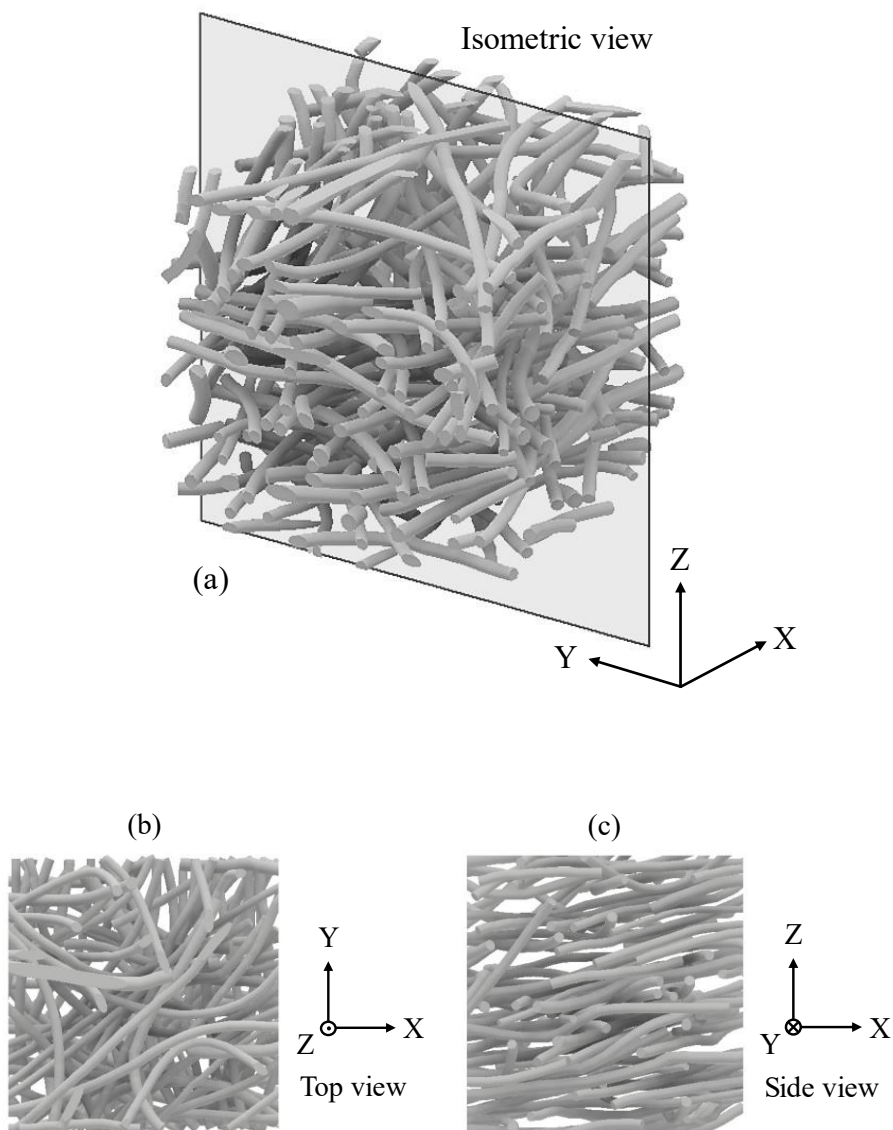


Figure 2.1 (a) Isometric view, (b) top view, and (c) side view of the 600 GSM PET felt. The gray square of the Fig. 2.1(a) coincides with the plane of micro-CT image plane.

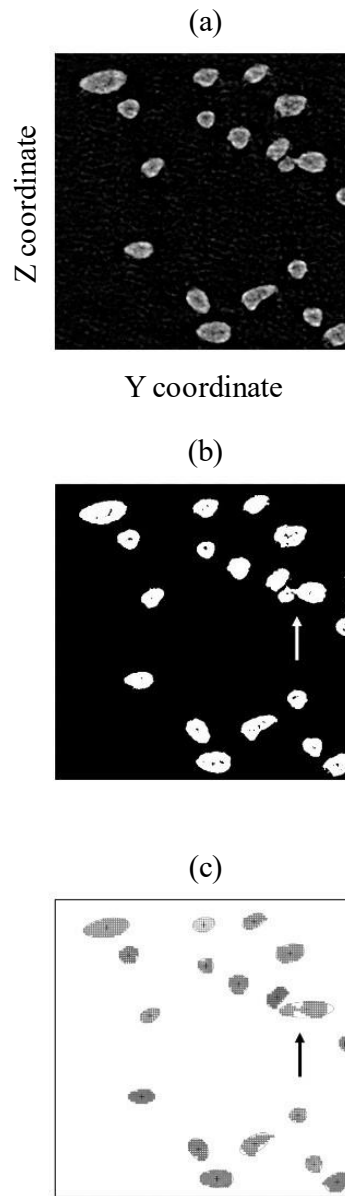


Figure 2.2 (a) Micro-CT raw image of PET felt, (b) binary threshold image, and (c) active points clustered using DB-SCAN.

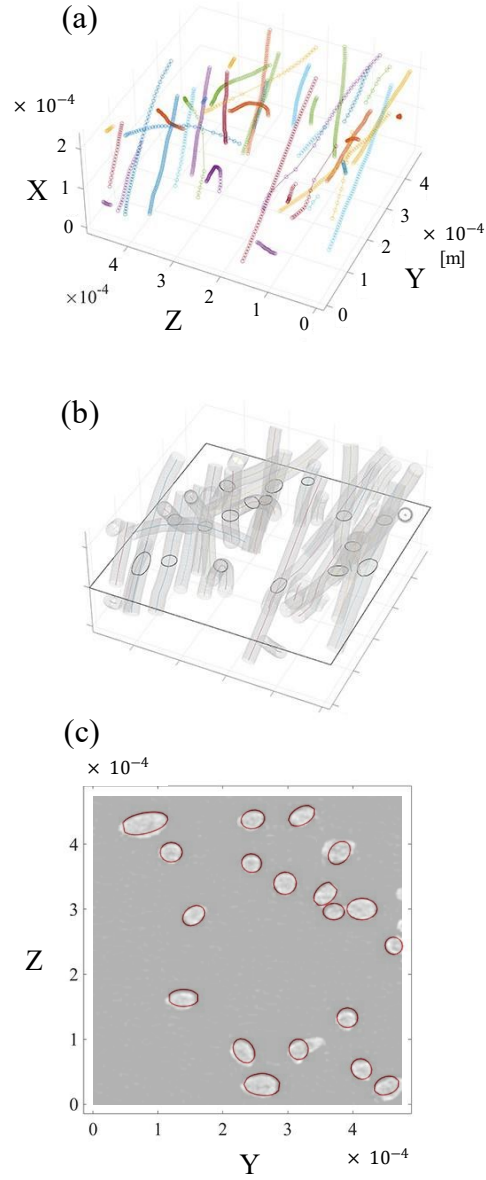


Figure 2.3 (a) Cluster centroid connections, (b) reconstruction of the 2-D geometrical model from the 3-D fiber model, and (c) overlaid image of the 2-D geometrical model and micro-CT image.

CHAPTER 3

EXPERIMENTAL PROCEDURES

3.1 Introduction

In this section, numerical experiments are applied to the 2-D geometrical model generated in chapter 2, and the process of obtaining the intrinsic parameters of each slice image is described. The five basic intrinsic parameters are covered required by the JCA model in this work. I employed the finite element method for a steady incompressible Stokes flow to obtain the static airflow resistivity [30, 31] and the boundary element method for a potential flow to obtain the tortuosity and VCL. [32, 33, 34] Porosity and TCL were obtained directly from the fiber geometry.

Chapter 3.2 introduces the process of obtaining intrinsic parameters using numerical experiments. Chapter 3.3 briefly discusses the process of obtaining parameters using direct measurement method, to verify the estimated values obtained in chapter 3.2. Finally, in chapter 3.4, the process of measuring the sound absorption coefficient is introduced. Here, the experimentally obtained sound absorption coefficient will be used to verify the predicted values in chapter 4 and 5.

3.2 Numerical experiments for obtaining intrinsic parameters

3.2.1 Model for porosity and thermal characteristic length

Porosity and TCL can be obtained using a mesh model constructed from the 2-D geometrical model, as shown in Fig. 3.1. First, the porosity ϕ can be calculated according to its definition as

$$\phi = \frac{1}{S_T} \sum_{i=1}^n S_i, \quad (3.1)$$

where S_i is the surface area of the i -th pore element, n is the total number of pore elements, and S_T is the total surface area of the mesh model, which is equal to $1000 \times 1000 \mu\text{m}^2$, as mentioned in chapter 2.

The TCL Λ' is defined as the ratio of the volume integration of the pore and the area integration of the fiber as

$$\Lambda' = 2 \frac{\int_V dV}{\int_S dS} \approx 2 \frac{\sum^n S_i}{\sum^m L_j \sqrt{2/(1 + \cos^2 \alpha)}}, \quad (3.2)$$

where L_j is the perimeter of the j -th fiber section on the plane and α is the

angle between the normal vector of the image plane and the fiber strand. α can be calculated as the ratio of the major and minor axis. Since this study deals with the 2-D flow field, volume integration was approximated by numerical area integration, and area integration was approximated by numerical line integration multiplied by a correction factor. When the fiber is positioned obliquely to the image plane in 3-D, the lateral area of the elliptical cylinder positioned perpendicular to the image plane is calculated if only the perimeter L_j is considered. Using the approximated perimeter of ellipse $p = 2\pi\sqrt{(a^2 + b^2)/2}$, (where a and b are the semi-major and semi-minor axis, respectively) the ratio of the lateral area between the elliptical cylinder and oblique cylinder can be obtained as $1:\sqrt{2/(1 + \cos^2\alpha)}$. The error resulting from this approximation will be presented in chapter 4.

3.2.2 Model for tortuosity and viscous characteristic length

Because the tortuosity and the VCL are defined in a flow of non-viscous fluid, [7] a potential flow analysis was conducted to obtain both parameters from the 2-D geometrical model. A uniform potential flow was made to flow with the velocity U_p from the left to the right side (z-axis direction) of the 2-D geometrical model, and the medium was assumed to be an incompressible

inviscid fluid. The upper and lower boundaries and the fiber contour were treated as impermeable walls. The description of the potential flow problem including applied boundary condition is given by

$$\nabla \cdot \mathbf{w}_P = 0 \text{ in } \Omega_f, \quad (3.3)$$

$$\nabla \times \mathbf{w}_P = 0 \text{ in } \Omega_f, \quad (3.4)$$

$$\mathbf{w}_P \cdot \mathbf{n} = 0 \text{ on } \Omega_{sf}, \quad (3.5)$$

where \mathbf{w}_P is the velocity of the fluid of the potential flow, Ω_f is the fluid domain, and Ω_{sf} is the fluid–solid interface, and \mathbf{n} is the unit normal to the boundary Ω_{sf} . Eq. (3.3) and (3.4) imply the incompressible and irrotational flow, respectively.

The flow field was calculated using the complex variable boundary element method. [19, 32, 33, 34] For a 2-D potential flow, the stream function Ψ is determined by

$$\mathbf{u} = \frac{\partial \Psi}{\partial y}; \text{ and } \mathbf{v} = -\frac{\partial \Psi}{\partial x}, \quad (3.6)$$

and if the 2-D incompressible flow is irrotational, the potential function Φ is

$$\mathbf{u} = \frac{\partial \Phi}{\partial x}; \text{ and } \mathbf{v} = \frac{\partial \Phi}{\partial y}. \quad (3.7)$$

Because Eq. (3.6) and (3.7) satisfy the Cauchy–Riemann condition, it is possible to form the complex potential W_P as a linear combination of Ψ and Φ as

$$W = \Phi + i\Psi. \quad (3.8)$$

The functions W, Φ, Ψ are all analytic, the velocity component $\mathbf{w}_P = (\mathbf{u}, \mathbf{v})$ can be obtained from W_P by differentiating with respect to z as

$$\frac{dW}{dz} = \mathbf{w}_P = \mathbf{u} - i\mathbf{v}. \quad (3.9)$$

The complex potential W_P at an arbitrary point z can be obtained with the Cauchy-type integral formula as

$$W(z) = \frac{1}{2\pi i} \oint_{\Omega_{sf}} \frac{W(\zeta)}{\zeta - z} d\zeta, \quad (3.10)$$

where ζ is a point on the boundary Ω_{sf} , $W(\zeta)$ takes on the values of the

potential and stream function along the boundary. Now, the boundary contour can be approximated by m discretized boundary elements. The nodal points located at both ends of the infinitesimal element are sequentially designated as ζ_1, ζ_2, \dots , and ζ_{m+1} . For a closed boundary, $\zeta_{m+1} = \zeta_1$. The Cauchy-type integral of Eq. (3.10) can be discretized as

$$W(z) = \sum_{j=1}^m \Delta_j W(z), \quad (3.11)$$

$$\Delta_j W(z) = \frac{1}{2\pi i} \int_{\zeta_j}^{\zeta_{j+1}} \frac{W(\zeta)}{\zeta - z} d\zeta, \quad (3.12)$$

where $\Delta_j W(z)$ is the contribution of the j -th infinitesimal element to the complex potential at an arbitrary point z .

The tortuosity α_∞ is defined as the ratio of the square of the path length in the porous material L_e to the square of the distance in free space L_0 , given by

$$\alpha_\infty = \left(\frac{L_e}{L_0} \right)^2. \quad (3.13)$$

The path length L_e can be obtained from the average length of the multiple

streamlines, where each individual streamline is found using the coordinates with equal stream function values in the flow field. [19] Excluding the stream function, which vanished on the fiber contour, the path length L_e was obtained from the length of the streamline maintained between both ends of the 2-D geometrical model. The horizontal length of the geometrical model was used as the distance in free space L_0 , and the tortuosity was calculated using Eq. (3.13). The streamline formed in the square box in Fig. 3.1 is shown in Fig. 3.2.

The viscous characteristic length Λ is defined by the ratio of the volume integration to the surface integration, in which each volume or area element is weighted according to the local value of the squared velocity field $|\mathbf{w}_P|^2$ as

$$\Lambda = 2 \frac{\int_V |\mathbf{w}_P(z)|^2 dV}{\int_S |\mathbf{w}_P(\zeta_{\Omega_{sf}})|^2 dS} \approx 2 \frac{\sum^n \int_S |\mathbf{w}_P(z)|^2 dS}{\sum^m \int_l |\mathbf{w}_P(\zeta_{\Omega_{sf}})|^2 dl}, \quad (3.14)$$

where $\int_S |\mathbf{w}_P(z)|^2 dS$ is the surface integration of the squared velocity of the pore element and $\int_l |\mathbf{w}_P(\zeta_{\Omega_{sf}})|^2 dl$ is the line integration of the squared velocity of the fiber contour element. For the similar reason as in the calculation of the TCL, volume integration and area integration are approximated by numerical area integration and line integration, respectively. However, when an ellipse on the plane exists due to the oblique fiber, it is difficult to inversely

estimate the difference in velocity field. Therefore, correction factor is not considered in this case. The error resulting from this assumption will be presented in chapter 4. The velocity field formed in the square box in Fig. 3.1 is shown in Fig. 3.3.

3.2.3 Model for static airflow resistivity

The flow field to obtain the static airflow resistivity is treated as a 2-D incompressible viscous air flow. The flow was applied as a steady, low Reynolds number flow. A viscous flow problem was solved using the Stokes flow, and the problem description including the Stokes equation and applied boundary conditions is shown in Eqs. (3.15)–(3.17), [22, 23]

$$\mu \nabla^2 \mathbf{w}_S - \nabla p = -\mathbf{G} \text{ in } \Omega_f, \quad (3.15)$$

$$\nabla \cdot \mathbf{w}_S = 0 \text{ in } \Omega_f, \quad (3.16)$$

$$\mathbf{w}_S = 0 \text{ on } \Omega_{sf}, \quad (3.17)$$

where μ is the viscosity of air, \mathbf{w}_S is the velocity of the fluid, p is the pressure, \mathbf{G} is the pressure gradient acting as a body force throughout the fluid domain. A laminar flow was made to flow from the left side to the right side (z-

axis direction) of the 2-D geometrical model. The boundary of the inlet and outlet was designated as the velocity U_S , and the upper and lower boundaries were treated as free slip conditions. The flow field was calculated using the finite element method. The fluid field of the geometrical model is discretized by a Taylor–Hood (P2-P1) triangular element that satisfies the Ladyzhenskaya-Babuška-Brezzi (LBB) condition, and the Galerkin method was applied to Eqs. (3.15)–(3.17). [19, 30, 31] The velocity and pressure field were obtained from a 2-D plane extended in the inlet and outlet direction of the 2-D geometrical model, and the spatially averaged pressure at both ends, $\langle P_{in} \rangle$ and $\langle P_{out} \rangle$, was calculated where the pressure field was sufficiently stabilized. The static airflow resistivity of the 2-D geometrical model was calculated using Darcy’s law given by

$$\sigma = \frac{\Delta p}{U_S L_0} , \quad (3.18)$$

where $\Delta p = \langle P_{in} \rangle - \langle P_{out} \rangle$ and L_0 is the length of the horizontal side of the geometrical model. The pressure field calculated from the geometrical model in Fig. 3.1 is shown in Fig. 3.4.

3.3 Intrinsic parameter measurement

The intrinsic parameters of PET were measured to validate the parameters predicted using the methods proposed in this work. Among the nine PET specimens, the parameters of three PETs used for testing the neural network were obtained using the direct measurement method and the inverse method. Testing PETs have surface densities of 800, 1000, and 1200 GSM, and the intrinsic parameters were measured for three specimens of each surface density. A brief summary of the measurement method is as follows, and the results are summarized in Table 3.1.

The porosity was measured using a porosity meter (PHI, Mecanum Inc., Quebec, Canada). The pressure and mass of the chamber were measured under four conditions: with and without a specimen in the chamber at an air pressure of less than 1.0 psi, and with and without a specimen in the chamber under pressure around 80 psi of argon gas. The porosity can be calculated from these four measurements using four ideal gas equations corresponding to these states. [16, 28]

The tortuosity was measured using a tortuosity meter (TOR, Mecanum Inc., Quebec, Canada). After measuring the impulse response with and without the specimen between the ultrasonic source and receiver sensors, the refraction

index of the material can be calculated using the phase difference between two impulse responses. By measuring the refraction index at multiple ultrasonic frequencies, the tortuosity can be calculated through high-frequency approximation using regression. [13]

The static airflow resistivity was measured in accordance with ISO 9053-1. [12] The pressure difference between the front and back sides of the specimen was measured while an air velocity of 1–10 mm/s flowed through the specimen. Then, the pressure difference was estimated at an air velocity of 0.5 mm/s using linear regression. The static airflow resistivity was then calculated using Darcy's law.

The TCL and VCL were obtained using the inverse characterization method. [42] The JCA model was used, and previously measured values of the parameters except for the two characteristic lengths were used. The normal incidence sound absorption coefficient required as the objective function of the inverse problem was measured using the Brüel and Kjær Type-4206 impedance tube, following the ASTM E1050 standard. [43]

3.4 Sound absorption coefficient measurement

The sound absorption coefficient of fibrous material was measured using a Bruel and Kjaer (B & K) two-microphone impedance tube (Type 4206). The B & K Type 4206 impedance tube consists of a loudspeaker, several microphone holders, and a cylindrical structure to mount a specimen. The sound reflection coefficient or the sound transmission loss can be measured using the transfer function between the microphones. [44, 45] After generating a broadband random signal in the frequency range of 100–6400 Hz, using a loudspeaker at one end of the tube, the transfer function between the two microphones is obtained over that frequency band. The sound reflection coefficient and the absorption coefficient can be calculated using the following transfer function:

$$H_{12} = \frac{P_2(\omega)}{P_1(\omega)} = \frac{P_i e^{jkx_2} + R(\omega)P_i e^{-jkx_2}}{P_i e^{jkx_1} + R(\omega)P_i e^{-jkx_1}}, \quad (3.19)$$

and

$$R(\omega) = \frac{e^{-jk(x_1-x_2)} - H_{12}}{H_{12} - e^{jk(x_1-x_2)}} e^{2jkx_1}, \quad (3.19)$$

where P_i is the incident wave in the impedance tube, $R(\omega)$ is the reflection coefficient, and x_1 and x_2 are the distance between the sample and the microphone locations, respectively (see Fig. 3.5 for more detail). When measuring the normal incidence sound absorption coefficient of a specimen using the B & K Type 4206, specimens with diameters of 100 mm and 29 mm can be used depending on the frequency range of interest. The suitable frequency range is 100 to 1600 Hz for 100 mm specimens and 500 to 6400 Hz for 29 mm specimens [46].

TABLE 3.1 Measured intrinsic parameters of the three testing PET specimens.

Testing PET	$\rho_{surface}$ [GSM]		ϕ [–]		α_{∞} [–]		σ [Nsm ^{−4}]		Λ' [μ m]	Λ [μ m]
	Mean	Std. Dev.	Mean	Std. Dev.	Mean	Std. Dev.	Mean	Std. Dev.	Inverse method	
A	800	20	0.863	0.010	1.04	0.03	69 500	1 100	106	33
B	1 000	20	0.847	0.008	1.09	0.04	103 000	2 800	84	27
C	1 200	20	0.825	0.009	1.14	0.07	121 000	5 100	74	24

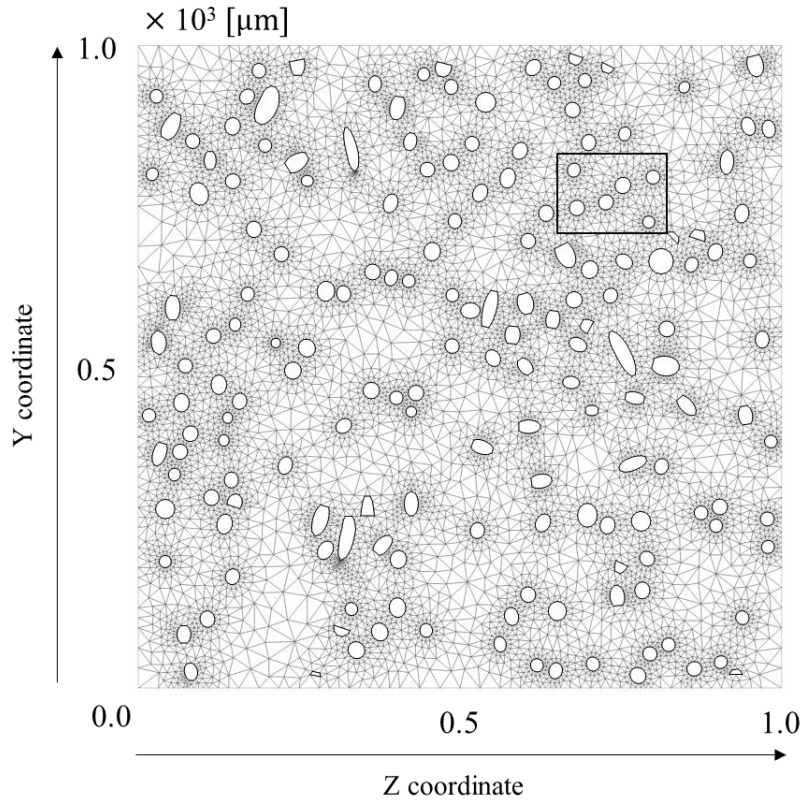


Figure 3.1 2-D mesh model constructed using the geometrical model. The square box in the figure is an area for visual reference of potential flow analysis to obtain tortuosity and VCL in Fig. 3.2 and Fig. 3.3.

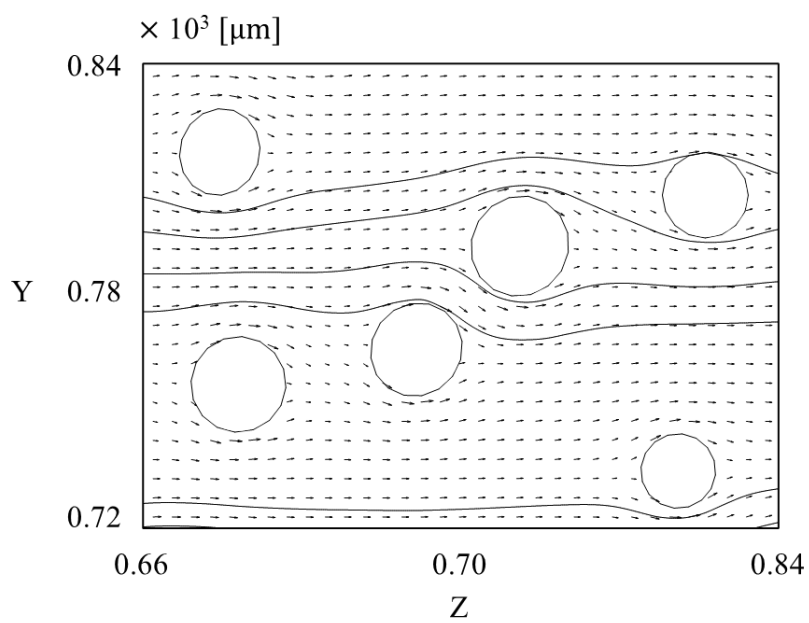


Figure 3.2 Streamlines of inviscid flow formed in the square box in Fig. 3.1.

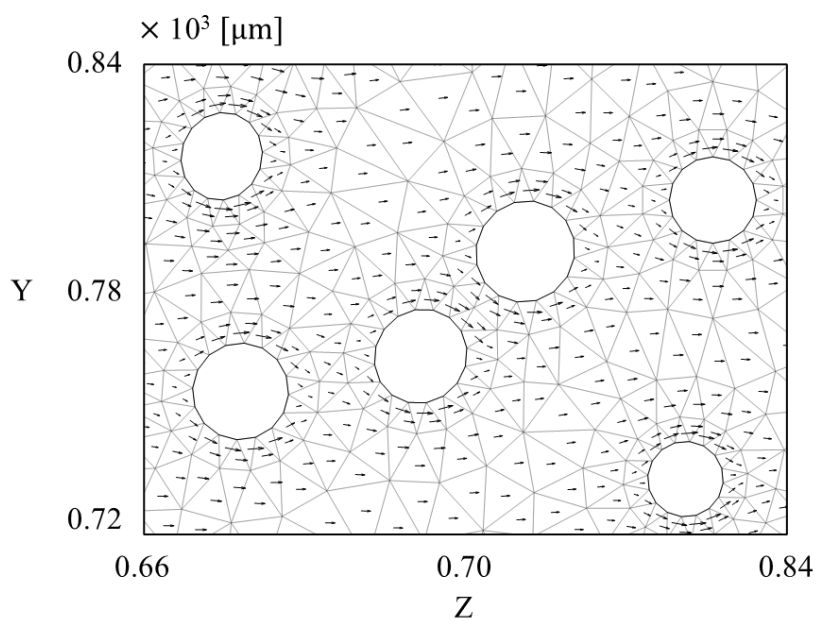


Figure 3.3 Velocity field of inviscid flow formed in the square box in Fig. 3.1.

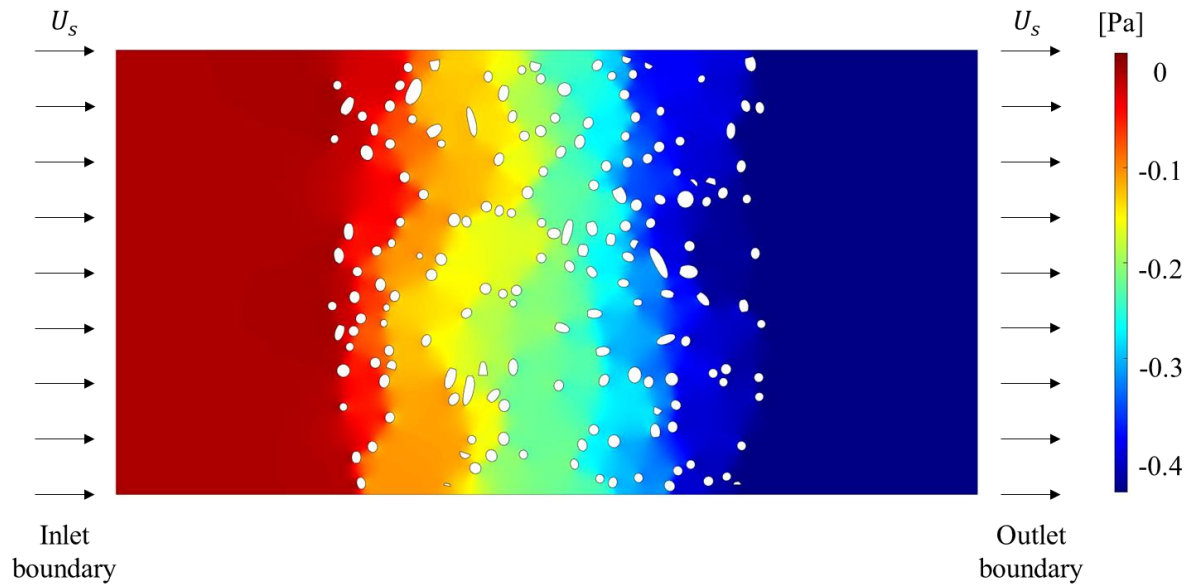


Figure 3.4 Analyzed pressure field from the 2-D geometrical model using stokes flow.

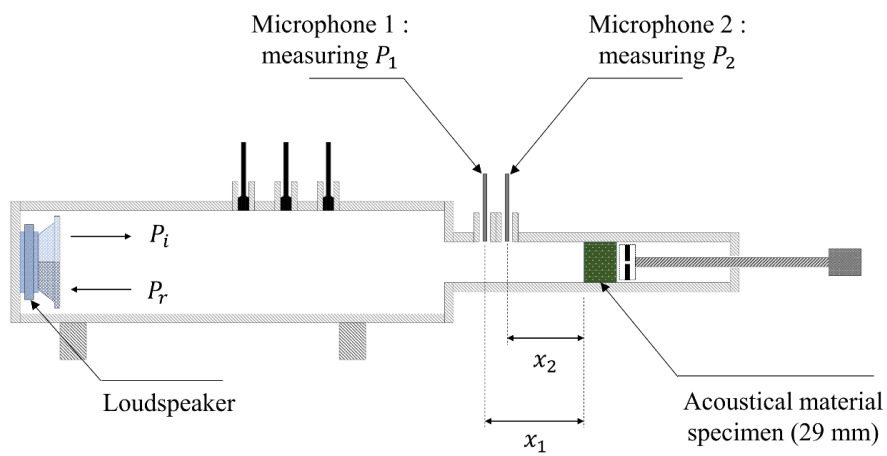


Figure 3.5 Schematic of the two-microphone impedance measurement tube (B & K Type 4206).

CHAPTER 4

NEURAL NETWORK MODEL DEVELOPMENT FOR INTRINSIC PARAMETERS OF FIBROUS MATERIAL

4.1 Introduction

The present chapter focuses on identifying the feasibility of an CNN model for estimating the intrinsic parameters of the fibrous materials. The objective of this work is to accurately estimate the intrinsic parameters of fibrous material by using the CNN models with 2-D micro-CT images as an input variable. The result will be compared with the value obtained using the transfer matrix method (TMM), which is widely used to obtain the acoustical properties of multi-layered porous media.

The concept of the neural network is briefly discussed in chapter 4.2, the modelling procedure is introduced in chapter 4.3. The validation of the developed CNN models is discussed in chapter 4.4, finally, the limitation of the developed model is noted in chapter 4.5.

4.2 Artificial neural network

4.2.1 Fully-connected artificial neural network

The configuration of a general feedforward ANN is shown in Fig. 4.1. The cubes in the figure represent artificial neurons, and the arrows represent the unidirectional calculation flow. The network can be divided into three layers: input layer, hidden layer, and output layer. For an arbitrary problem, once input and output variables are defined, the hidden layer serves to describe the relationship between them. In general, the number of layers and neurons is determined by the complexity of the data; however, the network normally consists of one input layer, one output layer, and one or more hidden layers. [47, 48]

The artificial neurons in the hidden and output layers are constructed similar to dendrites, cell bodies, and axons, which make up biological neurons. An example of the artificial neuron is shown in Fig. 4.2. Analogously to human neurons, each synaptic weight corresponds to the length of a dendrite, the summing junction corresponds to the cell body, and the activation function corresponds to the axon. The artificial neuron collects the information from previous neurons at the summing junction by multiplying synaptic weights and

adding a bias. For a given input, the artificial neurons calculate the activations as follows [49]:

$$x_j^n = \varphi \left(\sum_i w_{ji}^n x_i^{n-1} + b_j^n \right), \quad (4.1)$$

where $\varphi(x)$ represents the activation function, and x_i^{n-1} is the input of the i -th neuron in the $(n - 1)$ -th layer, x_j^n is the output of the j -th neuron in the n -th layer, w_{ji}^n is the synaptic weight from artificial neuron i in the $(n - 1)$ -th layer to neuron j in the n -th layer, and b_j^n is the respective bias term of the n -th layer. The most commonly used activation function is the rectified linear unit (ReLU): $\varphi(x) = \max(0, x)$. Nonlinear functions, such as the sigmoid $\varphi(x) = (1 + \exp(-x))^{-1}$ and \tanh , have been used in recent decades, but the ReLU function has been shown to give better results for complex and large networks [35].

The process of training a network constitutes optimization of the weights and biases of all neurons that make up the network through iterative learning from a given data set. The principle of optimizing weight and bias is based on the gradient descent method. Typically, the cost function in the regression problem can be set to a mean squared error (MSE), can be set as

$$f(\theta) = \frac{1}{N} \sum_{i=1}^N (\Theta_{\theta}(X_i) - Y_i)^2, \quad (4.2)$$

where $\Theta_{\theta}(X_i)$ is the predicted value of the neural network for a given input X_i , and Y_i is the observed value of the variable being predicted. The optimal set of weights and biases for a given input/output data minimizes MSE, $f(\theta)$, which can be found using the gradient descent method with numerical differentiation or backpropagation. [35, 50]

Since more complex networks require more computational resources to calculate gradients and costs, a mini-batch (a subset of a given dataset that is randomly chosen during training) can be used for efficient calculations. The method of obtaining gradients and costs via this mini-batch is called the stochastic gradient descent (SGD) method [51]. The procedure of updating weights and biases using SGD is defined as

$$W^{(t+1)} = W^{(t)} - \eta \nabla_W E(W^{(t)}), \quad (4.3)$$

where η is the step size, commonly known as a hyper parameter (the learning rate) in machine learning, t represents the current iteration indexed at zero. In addition to the SGD, various methods have been introduced that are used to

update the weights and biases [52, 53]. In this study, the adaptive moment estimation (Adam) method was used. In a complex model, solutions can be found faster and more efficiently using Adam than the SGD [54]. In the Adam algorithm, moving averages (averages that continually change as more data points are collected) of both the first moment and the second moment of the gradients are used. The updating algorithm of Adam is given by the following expressions [53]:

$$m_W^{(t+1)} = \beta_1 m_W^{(t)} + (1 - \beta_1) \nabla_W E(W^{(t)}), \quad (4.4)$$

$$v_W^{(t+1)} = \beta_2 v_W^{(t)} + (1 - \beta_2) \nabla_W E(W^{(t)}), \quad (4.5)$$

$$\hat{m}_W = \frac{m_W^{(t+1)}}{1 - \beta_1^{(t+1)}}, \quad (4.6)$$

$$\hat{v}_W = \frac{v_W^{(t+1)}}{1 - \beta_2^{(t+1)}}, \quad (4.7)$$

and

$$W^{(t+1)} = W^{(t)} - \eta \frac{\hat{m}_W}{\sqrt{\hat{v}_W} + \epsilon}, \quad (4.8)$$

where β_1 and β_2 are the hyper parameters of machine learning. These parameters adjust the damping ratio of the moving average. m_w represents the first moment of the gradient, v_w the second moment of the gradient and ϵ is a small scalar used to prevent division by zero.

The validation of the ANN is carried out using a test set, which is commonly extracted from a given data set or collected separately. Because the test set is unused for training the ANN, it can be used to evaluate the performance of the trained ANN. It functions to observe the potential overfitting problem of a network in the training process. If the ANN is overfitted on a training data set, it loses its generality when applied to unseen data, so the model needs to be evaluated using a test set.

4.2.2 Convolutional neural network

Fully connected networks generally use input variables in the form of a vector. Therefore, input variables of more than two dimensions, such as images, should be converted to a vector form when using a fully connected network. Two problems can arise during this process. First, if a 3-D variable such as an image (horizontal pixels, vertical pixels, and image channels) is converted into a one-dimensional (1-D) vector, the shape of the data is ignored. Here, the shape refers to a pattern formed by adjacent pixels or a similar color of spatially close pixels. Second, if a huge 2-D or 3-D input is converted into a 1-D vector, and fully connected with all the several hidden layers, the total number of weights and biases can be enormous. [29] To overcome this problem, I can use a 2-D CNN. The 2-D convolutional layer also has a network structure that includes weights and biases, similar to the fully connected layer. However, data flowing through the network is treated in the form of a 2-D matrix, and the weights are also expressed in the form of a 2-D matrix; this is called a filter or kernel. As shown in Eq. (11), the 2-D convolutional layer uses convolution of a 2-D matrix rather than a simple product of data and weight. The value of each element in the matrix can be calculated as

$$X^n = \varphi(X^{n-1} * W + b^n), \quad (4.9)$$

$$x_{ij}^n = \varphi \left(\sum_{p=0}^{m-1} \sum_{q=0}^{m-1} x_{(i+p)(j+q)}^{n-1} W_{(p+1)(q+1)} + b^n \right), \quad (4.10)$$

where X^{n-1} and X^n are the matrix forms of the input and output of the convolutional layer, respectively; W is a filter made up of weights; and x^{n-1} , x^n , and w are the elements of the matrices X^{n-1} , X^n , and W , respectively. The convolutional layer is generally used in combination with a pooling layer. Activation calculated in the convolutional layer is down-sampled in the pooling layer and then passed to the next layer. The pool size and stride values are determined in the pooling layer. [35]

4.3 Materials and model development

Six CNN models were trained to estimate the intrinsic parameters of a 2-D micro-CT slice image of a PET felt. Three of the six CNN models were trained to directly estimate the intrinsic parameters: (i) porosity, (ii) tortuosity, and (iii) static airflow resistivity of the 2-D image. The remaining three models were trained to estimate the three basic values in each 2-D slice image used to calculate the TCL and VCL of the bulk material. Each of the remaining three models estimates following values: (iv) summation of the line integration of the corrected fiber perimeter, $\sum \int_l dl$, which corresponds to the denominator in Eq. (3.2), (v) summation of the line integration of the squared velocity over the fiber skin, $\sum \int_l |v_{skin}|^2 dl$, which corresponds to the denominator in Eq. (3.14), and (vi) summation of the area integration of the squared velocity in the pore, $\sum \int_A |v_{pore}|^2 dA$, which corresponds to the numerator in Eq. (3.14). The summation of the area integration of the pore area, which corresponds to the numerator of Eq. (3.2) for calculating TCL, can be calculated by multiplying the area of the slice image by the porosity, so a separate model is not developed.

The dataset for training the CNN models was constructed using numerical analysis results and 2-D micro-CT slice images of six PETs, excluding the 800,

1000, and 1200 GSM PETs. Samples were extracted from three locations of each PET felt, and micro-CT images were obtained. One 3-D micro-CT image consists of $500 \times 500 \times 500$ voxels. Therefore, $500 \times 3 = 1500$ slice images per PET type were obtained, and 600 of the 1500 slice images were chosen for the numerical analysis. This procedure was performed in the same manner for six types of training PET for each surface density, for a total number of training datasets of $600 \times 6 = 3600$. The dataset for testing the CNN was constructed using the remaining three types of PET (800, 1000, and 1200 GSM). As in the previous procedure, three samples were taken for each PET type corresponding to each surface density. Of these, one sample was selected for each surface density and a numerical analysis was conducted. Thus, the total number of testing datasets was $500 \times 3 = 1500$.

The CNN architecture is shown in Table 4.1 and Fig. 4.3. The concepts of kernel size, stride, pool size, dropout layer, flatten, and batch normalization, which are not discussed in this paper, are explained in detail in the book by Buduma. [54] The structure of CNN model was designed by referring to ALEXNET, [55] although it is not identical. Each CNN model for predicting 6 parameters was made with the same structure. Here, the tuning of the structure and hyperparameter was ended through trial and error. Therefore, there may be a model that predicts the intrinsic parameters more accurately than the structure

of Table 4.1. Since the main goal of this study was confirming the feasibility of training the CNN model with the process of extracting the 2-D geometrical model from micro-CT image and numerical analysis, the CNN model was settled at upon determining that the degree of error was within the acceptable range. Training time for 3600 training set was approximately 24 h on 3.60 GHz/6 cores, 12 threads (128 GB RAM) for CNN model, and GPU was not used for training. The CNN in Fig. 4.3 is a model for predicting static airflow resistivity, and one filter of each convolutional layer is visualized in the middle of the layer. Through the visualized filter, it is possible to grasp the local pattern activated by the filter for the input array. As the layer becomes deeper in Fig. 4.3, the pore area and the fiber area are clearly divided and activated.

The cost function for training the CNN was chosen to be the MSE (Eq. (4.2)), and the gradient was calculated using backpropagation. The mini-batch size was set to 20, and weights and biases were optimized using the Adam algorithm with 0.001 learning rate. [53] The implementation was carried out using KERAS, which is a machine learning framework in PYTHON. The trend of the prediction error of the static airflow resistivity according to the number of training datasets is shown in Fig. 4.4. I employed the mean absolute percentage error (MAPE) for the relative comparison between the variables given by

$$\text{MAPE} = \frac{1}{N} \sum_{i=1}^N \left| \frac{\Theta_{\theta}(X_i) - Y_i}{Y_i} \right|, \quad (4.11)$$

Each variable is the same as in Eq. (4.2). The CNN model was checked by increasing the number of training datasets by increments of 300, and the MAPE was obtained using 1500 testing datasets for each step. When the number of training datasets reached 3600, the MAPE was confirmed to be around 2.5%, as shown in Fig. 4.4. Therefore, considering the computational cost and prediction accuracy of the model, the number of training datasets was set to 3600.

4.4 Model validation

The results of comparing the intrinsic parameters of 1500 testing images predicted using each CNN model and the values obtained using numerical analysis are shown in Fig. 4.5-7. The values obtained using numerical analysis are expressed as predicted value (Numerical) on the x-axis, and the predicted values of the CNN models are expressed on the y-axis. For each model, the MAPE and maximum error of the predicted values for 1500 testing images are shown at the bottom right of each figure. The MAPE of the predicted values from all six CNN models was less than 2.5%, and the maximum error was 8.87% in the static airflow resistivity model. The predicted results of the CNN models and the results of numerical analysis show good correlation. The results show that the CNN models have good prediction accuracy for new 2-D slice images. Fig. 4.8 shows the intrinsic parameters predicted using the CNN models corresponding to each slice image constituting the fibrous volume of one sample of testing PET B (1000 GSM), shown in Table 3.1. The dimension of fibrous volume is $1000 \times 1000 \times 1000 \mu\text{m}^3$.

When calculating the intrinsic parameters of the fibrous volume, porosity, tortuosity, and static airflow resistivity were calculated as the average of the predicted values from each slice image constituting the fibrous volume.

Because the tortuosity and static airflow resistivity are obtained from the potential flow and Stokes flow analysis in 2-D, respectively, the flow in the direction normal to the plane of the slice image inside the fibrous volume is ignored. In the Stokes flow analysis, because an incompressible fluid with a slow flow rate was assumed, it was considered that the same flow rate was inlet in all layers of each slice image constituting the fibrous volume. In the case of TCL, the volume integration of the pore and the area integration of the fiber of Eq. (3.2) corresponding to the fibrous volume were calculated by the summation of the pore area and the corrected perimeter of each slice image, respectively. Finally, in the case of VCL, the numerator and denominator terms in Eq. (3.14) corresponding to the fibrous volume are calculated by the summation of the area integration of the squared velocity in the pore and the line integration of the squared velocity over the skin of each slice image. Likewise, the fluid flow in the direction normal to the slice image is ignored in this process.

First, the change in the result according to the resolution of the image in the x-axis direction was investigated when configuring the fibrous volume. As shown in Fig. 4.9-10, it can be seen that the porosity is predicted to be larger than the actual value as the image resolution increases. (see Fig. 9 (a)) Accordingly, the static airflow resistivity tends to be small and the two

characteristic lengths to be large. It can be expected that as the resolution of the image gets closer to the diameter of the fiber strand, fibers cannot be captured within the resolution value. Therefore, it is important to set an appropriate resolution in consideration of the diameter of the fibers. Here, the analysis is performed using the 2 μm resolution.

Next, to confirm the generality of this method in which one of the directions of flow is ignored, it is necessary to investigate how much error occurs according to this approximation. To find the error, I used the reconstructed fiber model considering various fiber orientations by referring to the previous work. [25, 26] In the reconstructed model used by Luu *et al.*, [25] the azimuth angle of the fiber strand follows the uniform distribution, and the elevation angle follows the normal distribution. Therefore, the fiber model can be expressed with only one element of the second-order orientation tensor: Ω_{zz} (dimensionless quantity). Three models were constructed for each orientation angle set at 0.1 intervals from 0.0 to 1.0, and the results obtained by the numerical analysis of 3-D and 2-D slice geometrical models were compared. The porosity of each model was limited to 0.924 ± 0.003 , and the fiber radius and the number of fibers was as in the literature presented by Luu *et al.*. [26] The air flows along the +z direction and the 2-D slice geometry is extracted from the y-z plane along the x-axis. 3-D numerical analysis was conducted

using COMSOL Multiphysics, following the same problem definition as the 2-D problem. The cubic box dimension of the model was set as $500 \times 500 \times 500 \mu\text{m}^3$, and the 2-D slice geometry was extracted with a total of 101 sheets at $5 \mu\text{m}$ resolution. One thing to note is that unlike the PET felt consist of curved fibers, straight fibers are used in the reconstructed model. Therefore, when the angle between the y-z plane and the fiber is close to 0° , airflow on the 2-D geometry may be blocked. To avoid this problem, the fiber created with an angle between $\pm 3^\circ$ with the y-z plane was replaced with a fiber of an arbitrary angle. The maximum diameter of the fiber I used is $22.2 \mu\text{m}$, and the length of one edge of the cubic box is $500 \mu\text{m}$. When the azimuth angle of 68 fibers was initially created under uniform distribution, the number of fibers present in this angular range is 0 to 2.

The results are shown in Table 4.2. Only the mean percentage error (MPE) from comparing the mean parameters obtained from 3-D analysis with the parameters calculated by solving 2-D models was marked for intuitive understanding. For the porosity, the result of 3-D and 2-D analysis almost perfectly match. For the tortuosity, it shows an error within 5% in the whole range of the Ω_{zz} . As the Ω_{zz} increases, the static airflow resistivity obtained from 2-D analysis is found to be smaller than that from the 3-D analysis; and TCL and VCL are larger. Consequently, this method is valid within a limited

range, considering the error depending on the Ω_{zz} .

As mentioned in chapter 4.3, I took samples in three locations for each of the three types of testing PETs. The micro-CT images for each sample were input to the developed CNN models to obtain the intrinsic parameters for fibrous volume. The intrinsic parameters of the three testing PETs predicted using CNNs and the experimentally obtained values in chapter 3.3 are shown in Fig. 4.11-13. All predicted value and orientation angle of the testing PETs are shown in Table 4.3, with the error which is compared with mean of the measured values. The measured values and the estimated values have good correlation, whereas TCL and VCL show higher errors than the other three parameters. This was acceptable considering that the measured value was obtained by the inverse method. One thing to note is, due to the nature of the micro-CT image, it can be analyzed in two directions, y and z in the case of our micro-CT image. Even if the same image is used, inputting the image to the CNN in wrong direction can cause severe errors. For example, Ω_{zz} of the testing PET A #1 is 0.14, however Ω_{yy} is 0.46.

For further verification, 3-D models of all testing PETs were analyzed to compare with the results obtained from the CNN models. The actual 3-D fiber models were also constructed in the dimension of $500 \times 500 \times 500 \mu\text{m}^3$, extracted from the center of the fibrous volume used in the CNN model. Fig.

4.14 shows the 3-D geometrical model of testing PET B #1, streamlines inside the fiber obtained from the potential flow analysis, and the pressure field obtained from the Stokes flow analysis. The value of each intrinsic parameter obtained from the CNN and 3-D analysis are compared in Fig. 4.11-13, and Table 4.4 with the simulation time. The computational resource used in the analysis is same as mentioned in chapter 4.3, and the numerical analysis was conducted using COMSOL Multiphysics. Since the CNN models have the same structure, there is no significant difference in solving time for the analysis of different intrinsic parameters. Considering only the solving time, the CNN models take shorter time compared to numerical analysis. The required time considering the preparation time of materials in detail is described in Table 4.5.

Finally, the sound absorption coefficients of the testing PETs were calculated using the JCA model and the intrinsic parameters obtained, and the results were compared with the measured values, as shown in Fig. 4.15-17. Compared to the sound absorption coefficient using the experimentally measured intrinsic parameters, the sound absorption coefficient using the CNN models tended to be slightly lower overall, but it was confirmed that both values show good correlation with the sound absorption coefficient obtained using the impedance tube measurements.

4.5 Limitations of the model

Some limitations of this model should be noted. This study deals with a method of obtaining the intrinsic parameters of a 2-D image and predicting the parameters of the volume by stacking the images. In this process, the flow of fluid in the direction perpendicular to the image plane inside the material is ignored. Although this method reflects the changing fiber geometry in 3-D, it can obtain a meaningful result only when the ratio of the fiber perpendicular to the incident wave in the direction of the fiber is high. It is applicable to materials with directional properties such as glass wool or fibrous felt with a small orientation angle Ω_{zz} . One more limitation should be noted. In addition to the five parameters covered in this paper, one of the widely used parameter is the static thermal permeability. The JCA-Lafarge and JCA-Pride-Lafarge models require this parameter. The static thermal permeability can be obtained through heat transfer analysis, by solving the Poisson problem. [22, 25] Since there is a macroscopic one-directional flow in the fluid flow analysis, it was observed that an acceptable error was shown even if the flow in one direction inside the volume was ignored under limited condition. In contrast, in the case of heat transfer analysis, it is necessary to consider the heat transfer in all direction of the fiber geometry distributed in the volume in order to estimate the accurate

parameter. Therefore, it is difficult to estimate the static thermal permeability using the method presented in this study. However, once the micro-CT images are obtained, it is possible to construct the 3-D geometrical model. Also, the numerical analysis of the Poisson problem does not require a long solving time and computational resource for 3-D model as in the case of the Stokes problem. (less than 3 m for the actual 3-D fiber models with the computational resource used in this study) To present additional information related to this, I will briefly introduce the process of obtaining static thermal permeability.

The static thermal permeability k'_0 is a geometrical intrinsic parameter introduced by Lafarge *et al.*, which describes the thermal exchanges between the solid frame and fluid. [11] The static thermal permeability can be obtained solving the Poisson problem, and the description of the problem including applied boundary condition is given by

$$\nabla^2 \cdot \mathbf{u} = -1 \text{ in } \Omega_f, \quad (3.3)$$

$$\mathbf{u} = 0 \text{ on } \Omega_{sf}, \quad (3.4)$$

where \mathbf{u} is a temperature field for the heat diffusion problem. The thermal permeability can be obtained as the fluid-phase average of the \mathbf{u} . The numerical analysis to obtain the thermal permeability of 2-D and 3-D models

is described in more detail in the previous literature. [22, 25, 56]

As mentioned above, the effect of thermal exchange along all directions in 3-D fibrous volume should be considered to estimate the static thermal permeability. To support this point, a numerical experiment was conducted using a single fiber strand passing through the center of a $100 \times 100 \times 100 \mu\text{m}^3$ cubic box. The elevation angle, which is the angle between the fiber and z-axis, was set to 90° (i.e., $\Omega_{zz} = 0$), azimuth angle to 0° , and fiber diameter to $25 \mu\text{m}$, as the initial conditions. Under these conditions, the porosity is equal to 0.951. Subsequently, a heat diffusion analysis was conducted using 3-D and 2-D slice geometries by decreasing the elevation angle of the fiber by 10° intervals. For 2-D analysis, 11 slice geometries were extracted at $10 \mu\text{m}$ intervals along the x-axis of the cubic box. To consider the porosity of all models consistently, the diameter of the fiber was gradually decreased with the elevation angle, and the azimuth angle was fixed at 0° . The errors of static permeability obtained from 2-D analysis at the elevation angle in the range of 90° to 50° are summarized in Table 4.6. For comparison, the error of the static airflow resistivity and VCL are also indicated. The direction of air flow is the z-direction. A heat diffusion analysis was conducted using a 3-D model of testing PETs to convey additional information. The obtained static thermal permeability of each model is summarized in Table 4.7. The pattern of scaled

heat diffusion field shown in Fig. 4.18 supports that the effect of 3-D thermal exchange must be considered to estimate the static thermal permeability.

Finally, the output value of the CNN model is designated as a intrinsic parameter in this work for connection with the acoustic impedance model such as the JCA model used conventionally. However, if the desired output value is an acoustic property such as sound absorption coefficient, it will be possible to develop a model considering that the impedance model is also included in the hidden layer of the neural network in future work. Also, unlike using micro-CT image as an input value in this work, other image information that can be obtained more simply can be considered. For example, a scanning electron microscope (SEM) image taken from a specific direction can be used as an input value, and acoustic properties such as the sound absorption coefficient, sound transmission loss, and sound insertion loss can be used as an output value.

TABLE 4.1 Detailed layer information of the developed CNN model architecture.

Layer	Layer type and activations	Input size	Output size
1	Input	$500 \times 500 \times 1$	
	Convolutional layer [kernel size = 5×5 , strides = (1, 1), 16 filters] + ReLU	$500 \times 500 \times 1$	$500 \times 500 \times 16$
	+ MaxPooling [pool size = 2×2 , strides = (2, 2)]	$500 \times 500 \times 16$	$250 \times 250 \times 16$
2	Convolutional layer [kernel size = 2×2 , strides = (2, 2), 32 filters] + ReLU	$250 \times 250 \times 16$	$250 \times 250 \times 32$
	+ MaxPooling [pool size = 2×2 , strides = (2, 2)]	$250 \times 250 \times 32$	$125 \times 125 \times 32$
3	Convolutional layer [kernel size = 2×2 , strides = (2, 2), 64 filters] + ReLU	$125 \times 125 \times 32$	$125 \times 125 \times 64$
	+ MaxPooling [pool size = 2×2 , strides = (2, 2)]	$125 \times 125 \times 64$	$62 \times 62 \times 64$
4	Dropout (0.25) + Flatten + Fully connected layer + Batch normalization + ReLU	$62 \times 62 \times 64$ 246 016	246 016 300
5	Fully connected layer + Batch normalization + ReLU	300	200
6	Fully connected layer + Batch normalization + ReLU Output	200	100 1

TABLE 4.2 Errors between the 3-D and 2-D numerical analysis of the reconstructed fiber models according to the orientation angles.

Ω_{zz}	ϕ		α_{∞}		σ		Λ'		Λ	
	3-D	2-D stack	3-D	2-D stack	3-D	2-D stack	3-D	2-D stack	3-D	2-D stack
	Value [-]	MPE [%]	Value [-]	MPE [%]	Value $\times 10^3$ [Nsm $^{-4}$]	MPE [%]	Value [μ m]	MPE [%]	Value [μ m]	MPE [%]
0.0	0.923	0.0	1.04	(+) 2.9 \pm 0.8	42.6	(-) 4.0 \pm 1.7	134.5	(+) 0.7 \pm 0.3	74.2	(+) 4.9 \pm 0.3
0.1	0.925	0.0	1.03	(+) 4.1 \pm 1.3	39.7	(-) 3.1 \pm 1.3	136.4	(+) 0.3 \pm 0.2	77.2	(+) 3.9 \pm 2.1
0.2	0.925	0.0	1.03	(+) 3.9 \pm 0.0	37.3	(-) 1.8 \pm 1.1	137.2	(+) 1.1 \pm 0.2	81.0	(+) 2.7 \pm 1.7
0.3	0.925	0.0	1.02	(+) 4.2 \pm 0.9	36.6	(-) 3.7 \pm 1.7	138.5	(+) 0.4 \pm 0.3	83.8	(+) 4.0 \pm 1.8
0.4	0.925	0.0	1.02	(+) 3.6 \pm 0.5	35.5	(-) 9.0 \pm 4.5	138.4	(+) 0.9 \pm 0.7	89.7	(+) 3.9 \pm 1.8
0.5	0.925	0.0	1.02	(+) 3.5 \pm 0.5	33.1	(-) 10.4 \pm 1.1	136.8	(+) 1.9 \pm 0.7	96.2	(+) 4.9 \pm 0.9
0.6	0.925	0.0	1.01	(+) 4.5 \pm 0.5	30.1	(-) 11.6 \pm 2.5	137.4	(+) 1.0 \pm 0.2	98.4	(+) 3.6 \pm 0.5
0.7	0.925	0.0	1.01	(+) 3.3 \pm 0.0	37.9	(-) 19.8 \pm 0.7	136.2	(+) 3.1 \pm 0.1	106.0	(+) 5.7 \pm 2.2
0.8	0.924	0.0	1.00	(+) 2.6 \pm 0.1	25.7	(-) 36.6 \pm 2.0	134.2	(+) 5.4 \pm 0.6	113.4	(+) 15.5 \pm 2.3
0.9	0.923	0.0	1.00	(+) 2.9 \pm 0.1	24.8	(-) 43.9 \pm 4.9	134.7	(+) 7.6 \pm 0.8	121.4	(+) 31.8 \pm 3.9
1.0	0.924	0.0	1.00	0.0 \pm 0.0	21.6	(-) 74.0 \pm 7.2	136.4	(+) 13.6 \pm 1.1	136.4	(+) 64.9 \pm 4.5

TABLE 4.3 Intrinsic parameters predicted using CNNs of the three samples of each testing PET and error from the mean of measured value.

Testing PET		Ω_{zz}	ϕ [–]	α_{∞} [–]	σ [Nsm ⁻⁴]	Λ' [μm]	Λ [μm]
A	#1	0.14	0.865	1.09	73 900	89	40
	#2	0.13	0.862	1.03	71 800	82	38
	#3	0.11	0.850	1.04	74 100	80	36
Mean		0.13	0.859	1.05	73 300	84	38
Std. Dev.		0.01	0.006	0.03	1 000	4	2
Error [%]			0.5	1.0	5.5	20.8	15.2
B	#1	0.11	0.843	1.07	96 000	74	32
	#2	0.12	0.841	1.09	102 000	73	31
	#3	0.10	0.840	1.10	101 000	68	30
Mean		0.11	0.841	1.09	99 700	72	31
Std. Dev.		0.01	0.001	0.01	2 600	3	1
Error [%]			0.7	0.0	3.2	14.3	14.8
C	#1	0.10	0.824	1.11	110 000	64	29
	#2	0.07	0.816	1.12	112 000	63	26
	#3	0.09	0.815	1.11	122 000	61	26
Mean		0.09	0.818	1.11	115 000	63	27
Std. Dev.		0.01	0.004	0.01	5 200	1	1
Error [%]			0.8	2.6	5.0	14.9	12.5

TABLE 4.4 Comparison of the estimated intrinsic parameters and solving time between the 3-D numerical analysis and CNN model analysis for testing PETs.

Testing PET		ϕ [–]	α_{∞} [–]	σ [Nsm ⁻⁴]	Λ' [μm]	Λ [μm]	Averaged solving time	
							Potential flow	Stokes flow
PET A:	3-D	0.860	1.04	76 000	83	36	6 m	17 h
800	CNNs	0.859	1.05	73 300	84	38	15 s	15 s
[GSM]	Error [%]	0.1	1.0	3.6	1.2	5.6		
PET B:	3-D	0.841	1.08	102 000	72	30	12 m	47 h
1 000	CNNs	0.841	1.09	99 700	72	31	15 s	15 s
[GSM]	Error [%]	0.0	0.9	2.3	0.0	3.3		
PET C:	3-D	0.820	1.10	122 000	64	26	15 m	66 h
1 200	CNNs	0.818	1.11	115 000	63	27	15 s	15 s
[GSM]	Error [%]	0.2	0.9	5.7	1.6	3.8		

TABLE 4.5 Detailed information on micro-CT image acquisition, modelling, and computation time.

2-D convolutional neural network (5 000 images in this work)		3-D numerical analysis (5 volumetric samples in this work)	
Collecting Micro-CT image	24 h / 1 sample	24 h / 1 sample	
Modelling time	2-D geometrical modelling	1 week / 5 000 images	
	2-D numerical analysis	3 weeks / 5 000 images	3-D geometrical modelling
	CNN modelling	24 h / 1 model (total 6 models are developed)	3 days / 1 sample
	Total time	5 weeks	Total time 15 days
Computation time	15 s / 1 parameter	Stokes flow problem	60 h ~ 120 h
		Potential flow problem	10 m ~ 20 m

TABLE 4.6 Error of the intrinsic parameters obtained using 2-D slice geometries of the single fiber strand model.

	Error of 2-D analysis [%]				
	90°	80°	70°	60°	50°
k'_0	0.0	2.8	11.8	27.8	53.4
σ	0.4	0.5	0.5	0.3	3.1
Λ	0.0	0.2	0.5	0.5	1.2

TABLE 4.7 The static thermal permeability of testing PETs obtained using 3-D heat transfer analysis.

Testing PET		ϕ [–] of 3-D model	k'_0 $\times 10^{-11}$ [m ²]
A	#1	0.865	57.4
	#2	0.862	54.2
	#3	0.852	46.3
	Mean	0.860	52.6
	Std. Dev.	0.006	4.7
B	#1	0.843	41.0
	#2	0.841	44.4
	#3	0.840	39.4
	Mean	0.841	41.6
	Std. Dev.	0.001	2.1
C	#1	0.826	34.7
	#2	0.816	27.1
	#3	0.817	30.3
	Mean	0.820	30.7
	Std. Dev.	0.004	3.1

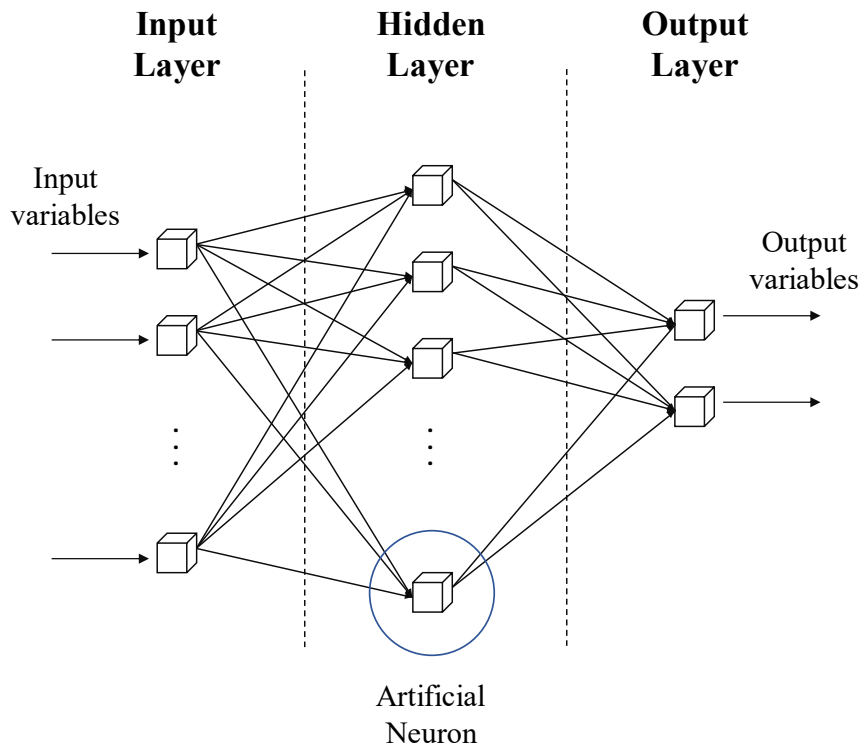


Figure 4.1 Schematic architecture of a typical feedforward neural network.

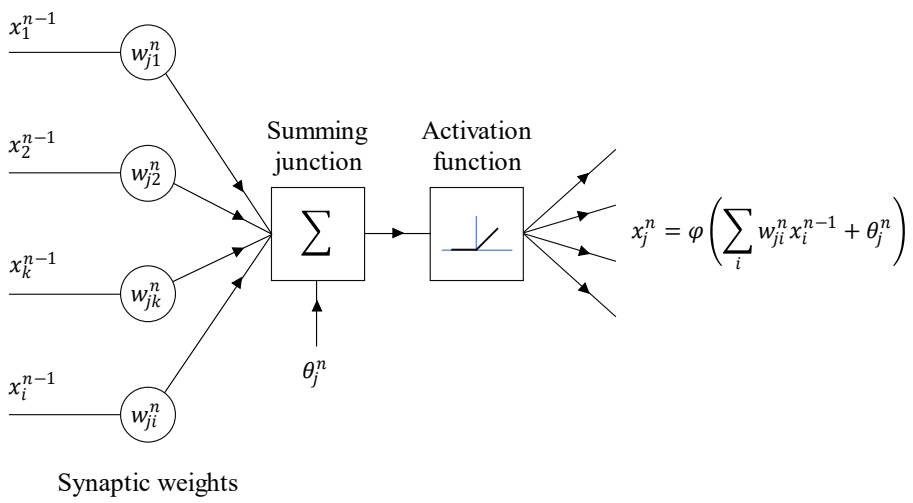


Figure 4.2 Detailed structure of an artificial neuron.

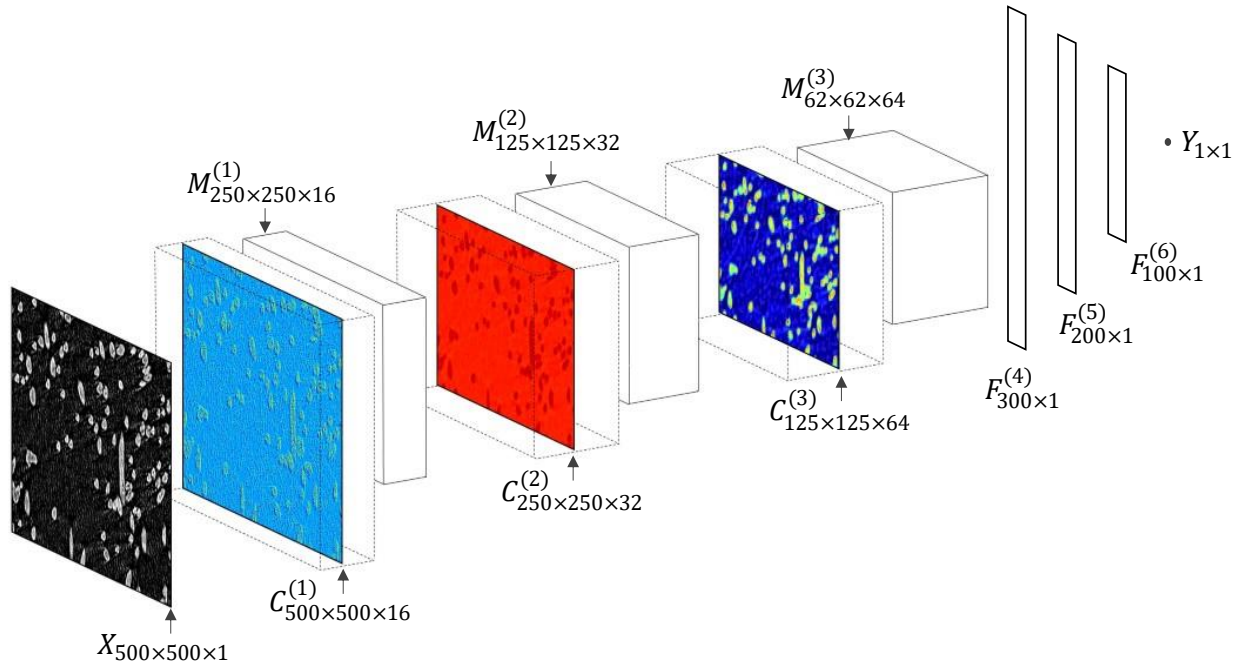


Figure 4.3 6-layer (3-convolutional layer, 3-fully connected layer) architecture of the CNN model for AFR.

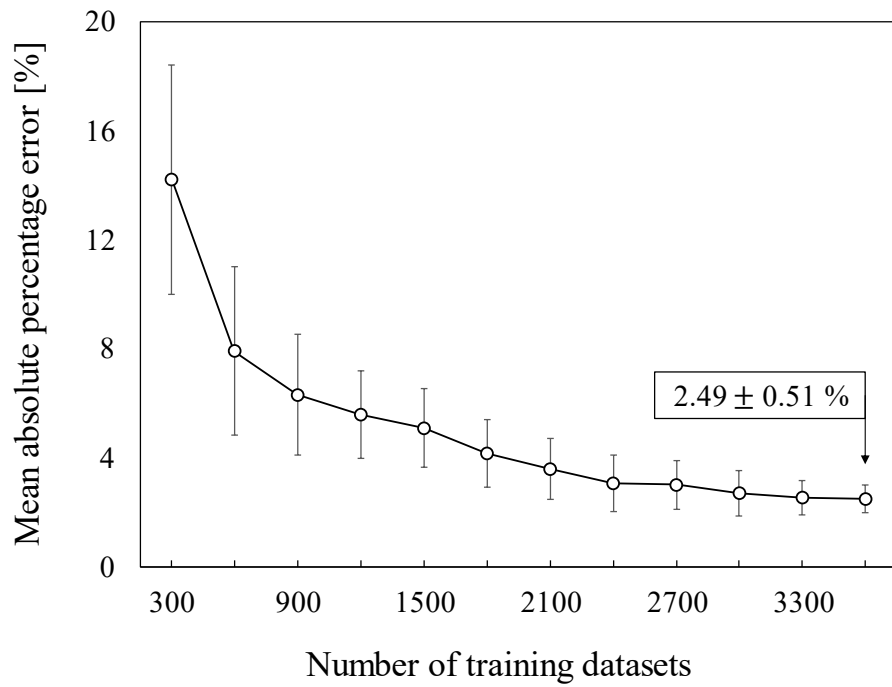


Figure 4.4 The trend of prediction error of static airflow resistivity according to the number of training datasets.

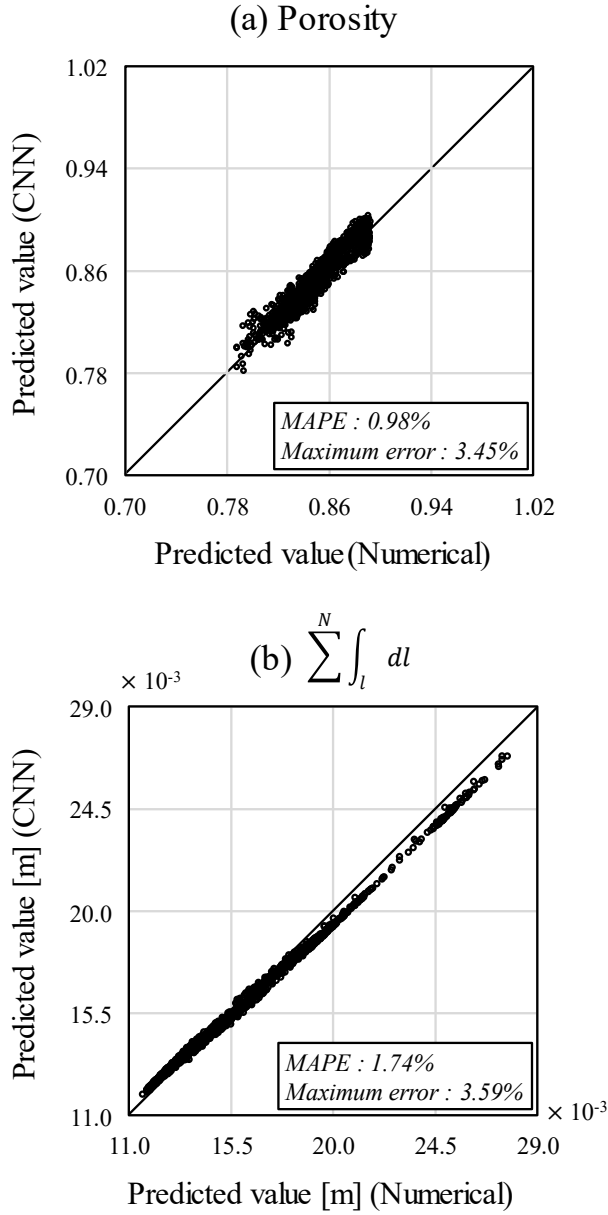


Figure 4.5 (a) Porosity and (b) summation of the line integration of the corrected fiber perimeter of 1500 testing images predicted using each CNN model and the values obtained using numerical analysis.

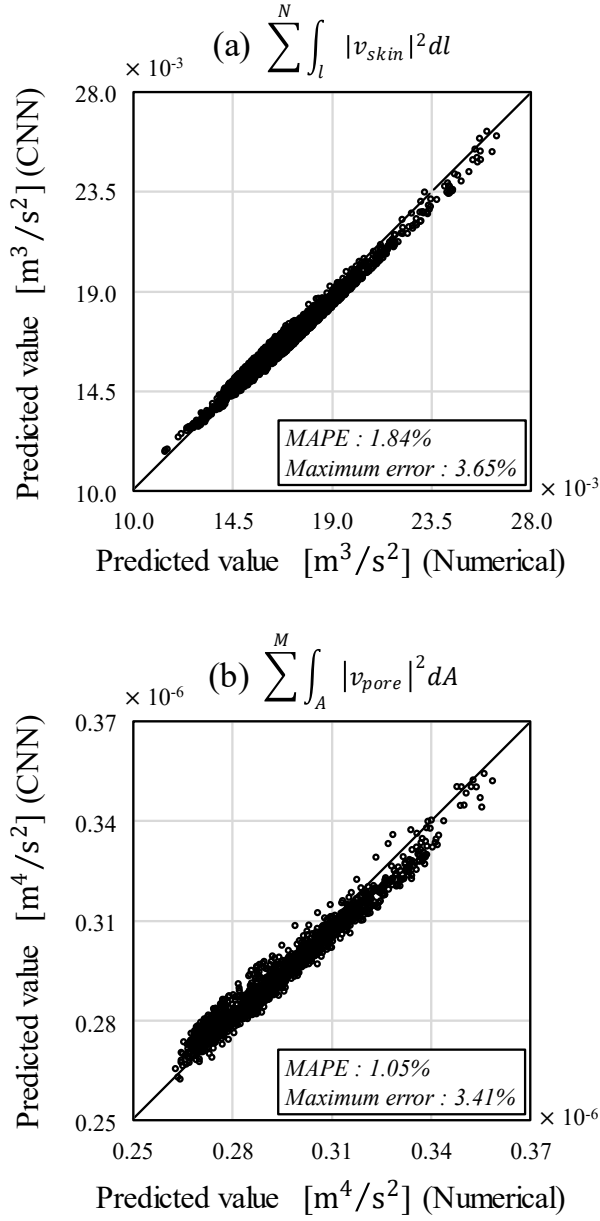


Figure 4.6 (a) Summation of the line integration of the squared velocity over the fiber skin and (b) summation of the area integration of the squared velocity in the pore of 1500 testing images predicted using each CNN model and the values obtained using numerical analysis.

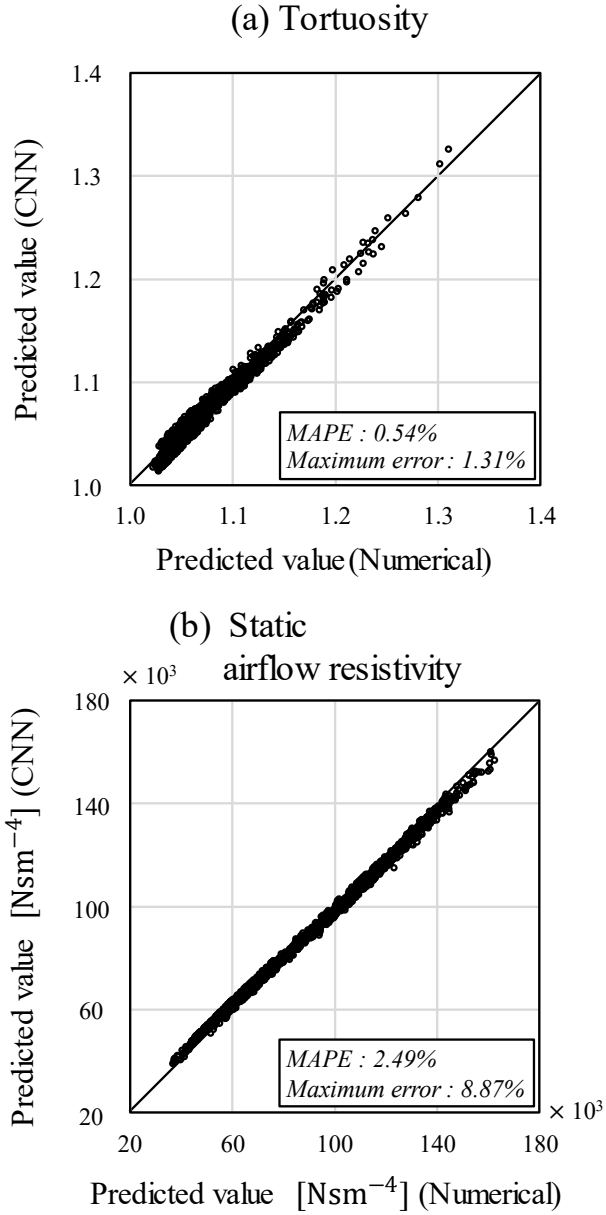


Figure 4.7 (a) Tortuosity and (b) static airflow resistivity of 1500 testing images predicted using each CNN model and the values obtained using numerical analysis.

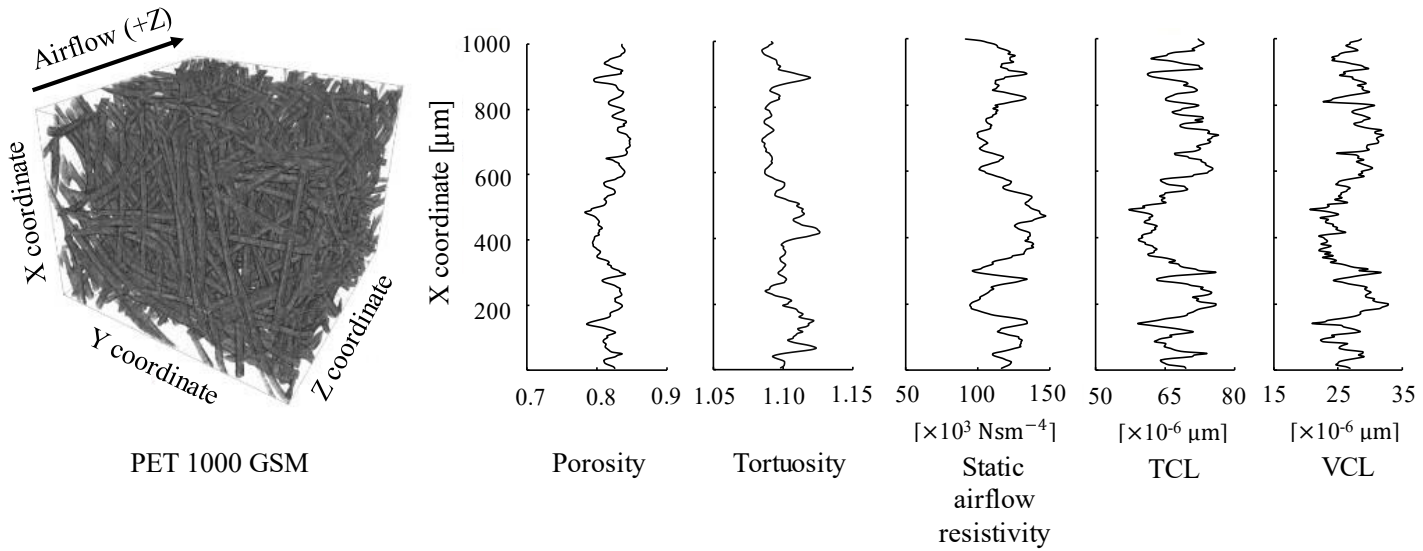


Figure 4.8 The intrinsic parameters predicted using CNNs corresponding to each slice image constituting the fibrous volume.

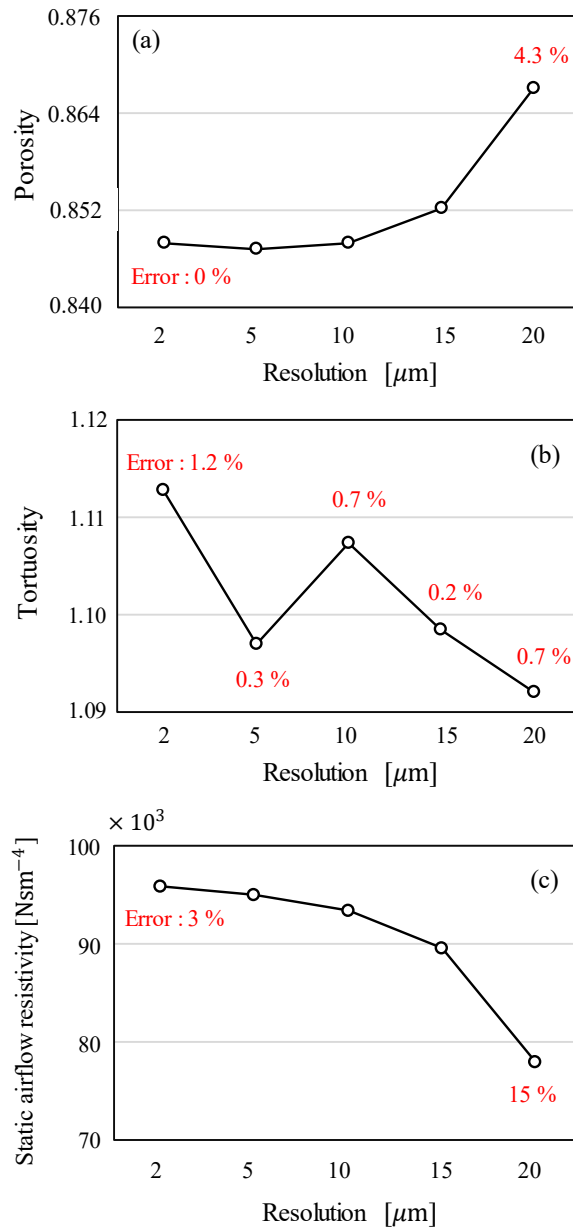


Figure 4.9 Change of intrinsic parameter values according to x-axis image resolution; (a) porosity, (b) tortuosity and (c) static airflow resistivity.

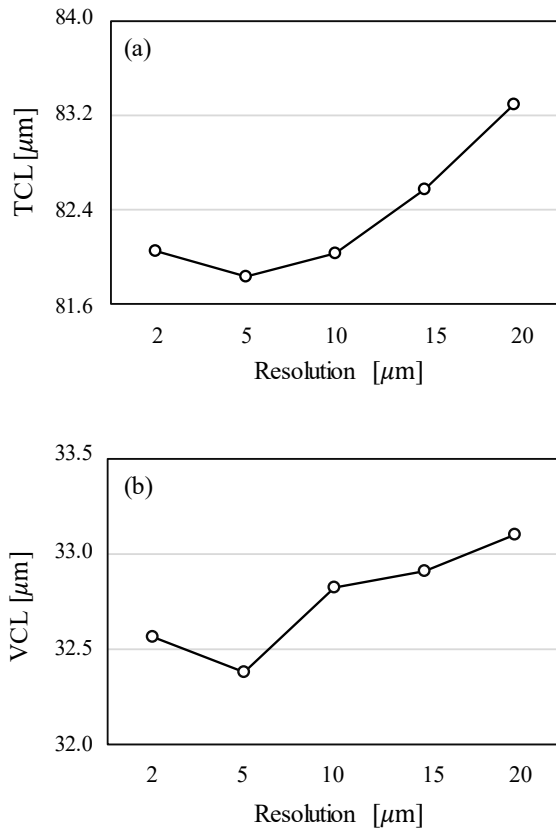


Figure 4.10 Change of intrinsic parameter values according to x-axis image resolution; (a) TCL and (b) VCL.

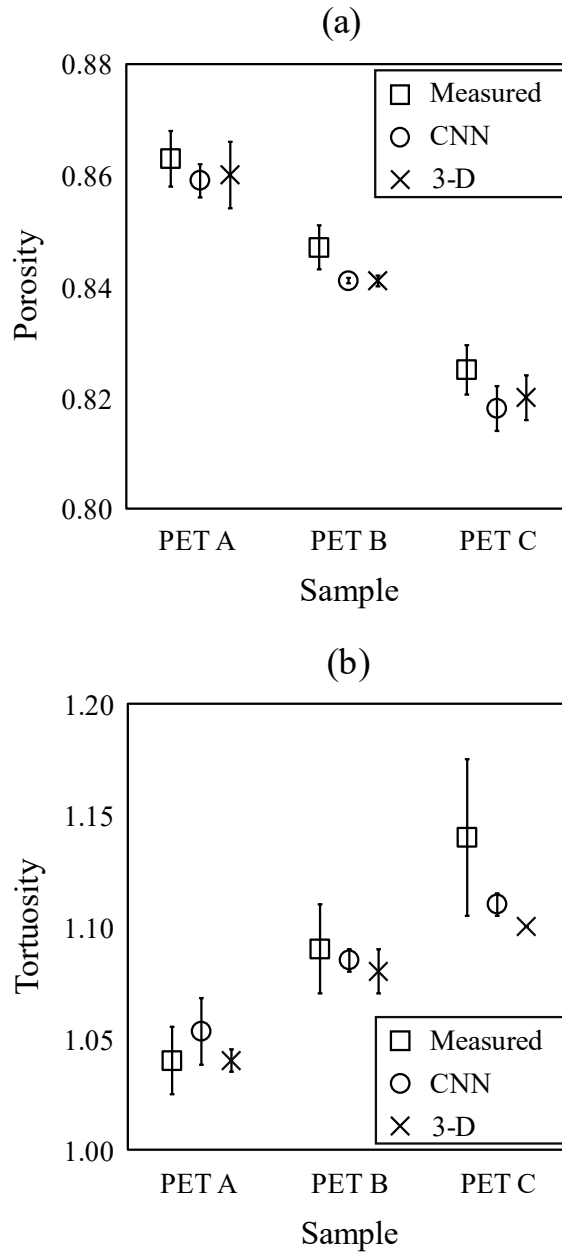


Figure 4.11 Comparison of measured and predicted intrinsic parameters; (a) porosity and (b) tortuosity.

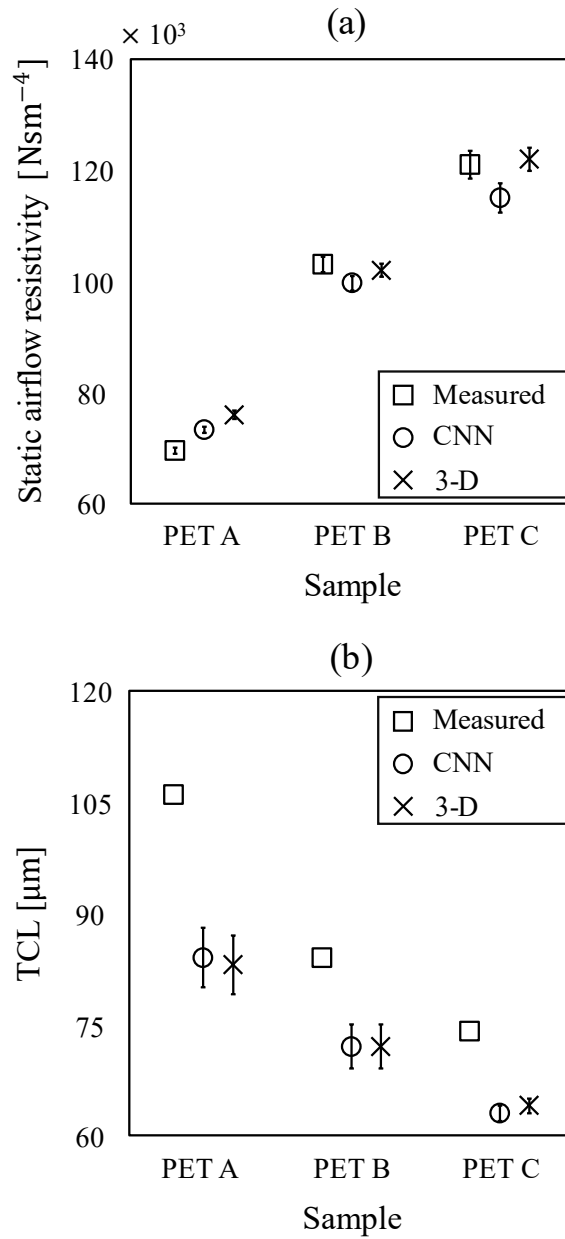


Figure 4.12 Comparison of measured and predicted intrinsic parameters; (a) static airflow resistivity and (b) thermal characteristic length.

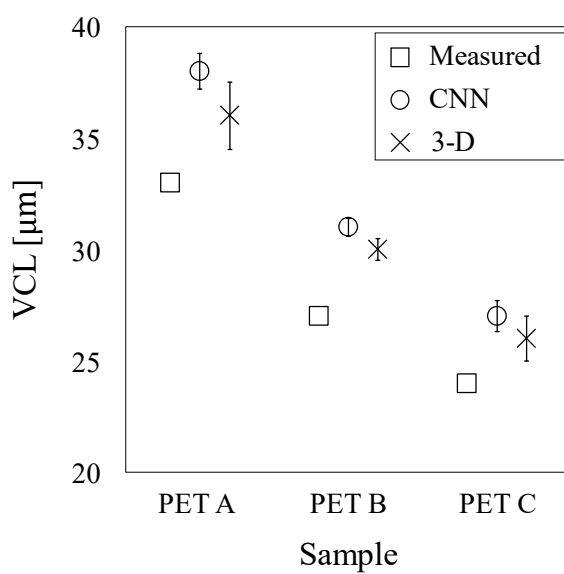


Figure 4.13 Comparison of measured and predicted intrinsic parameters; viscous characteristic length.

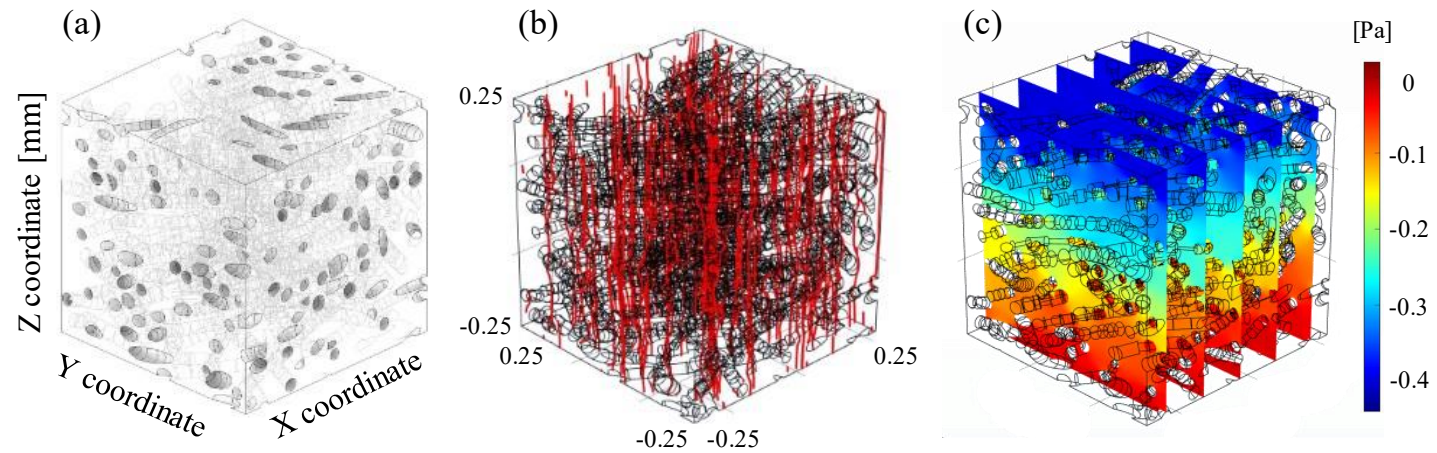


Figure 4.14 (a) 3-D geometrical for testing PET B #1 (b) streamlines obtained from potential flow analysis, (c) pressure field obtained from Stokes flow analysis.

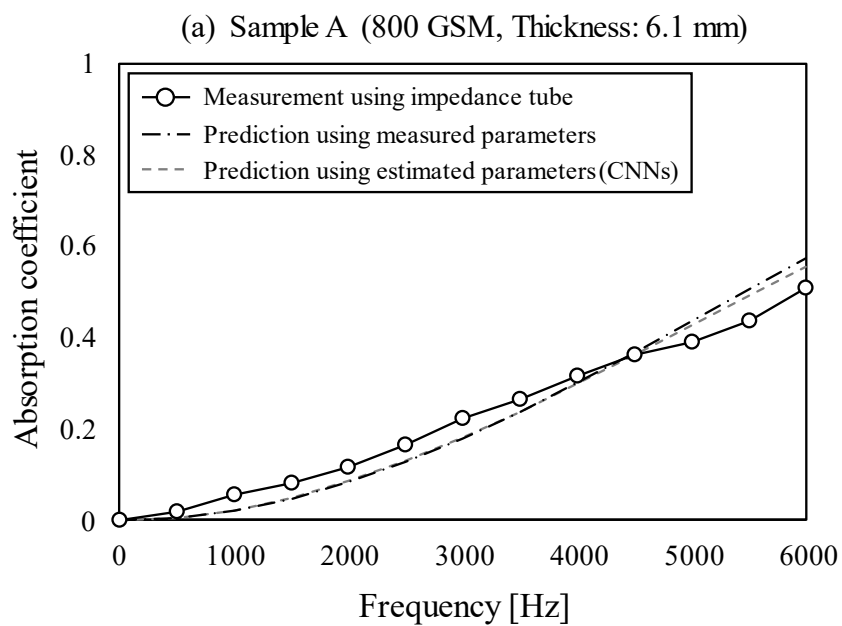


Figure 4.15 Normal incidence sound absorption coefficient of the PET A.

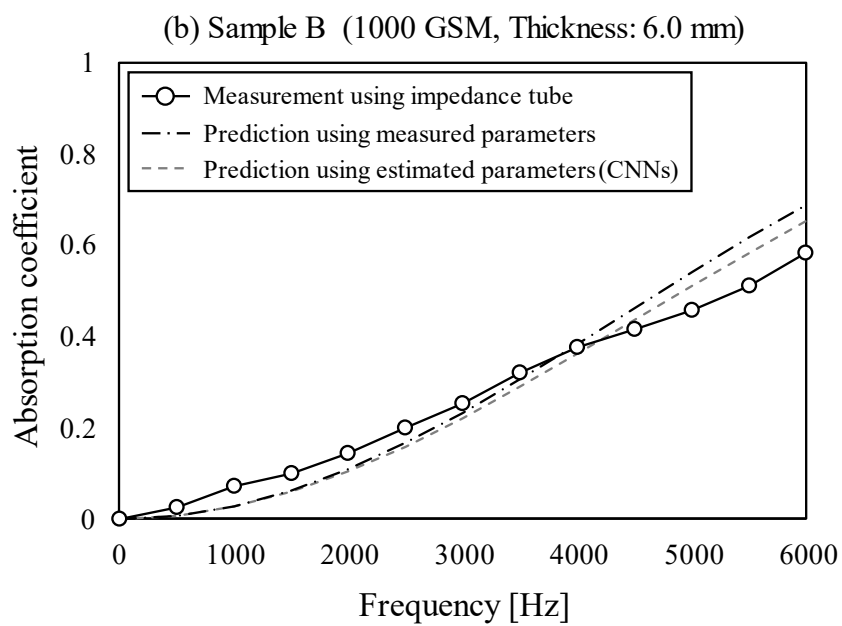


Figure 4.16 Normal incidence sound absorption coefficient of the PET B.

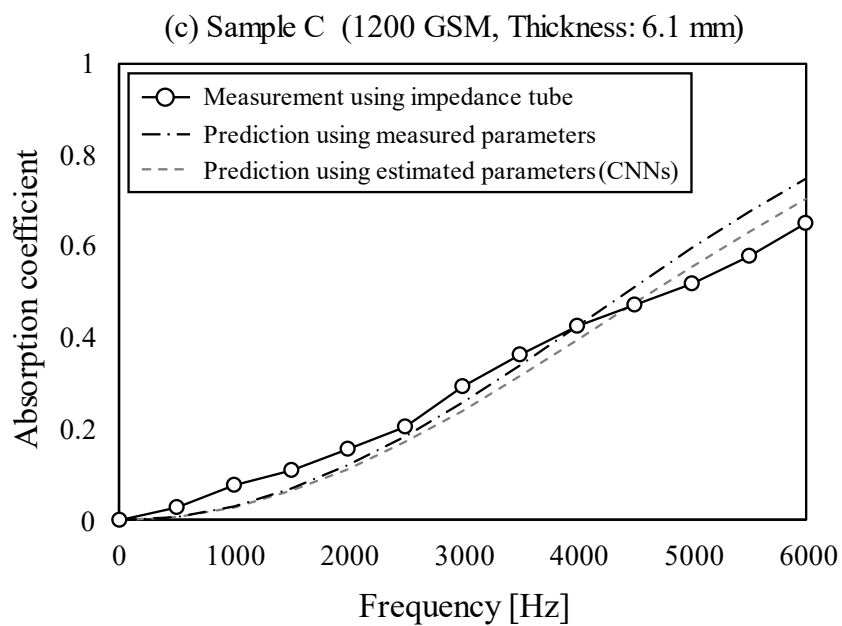


Figure 4.17 Normal incidence sound absorption coefficient of the PET C.

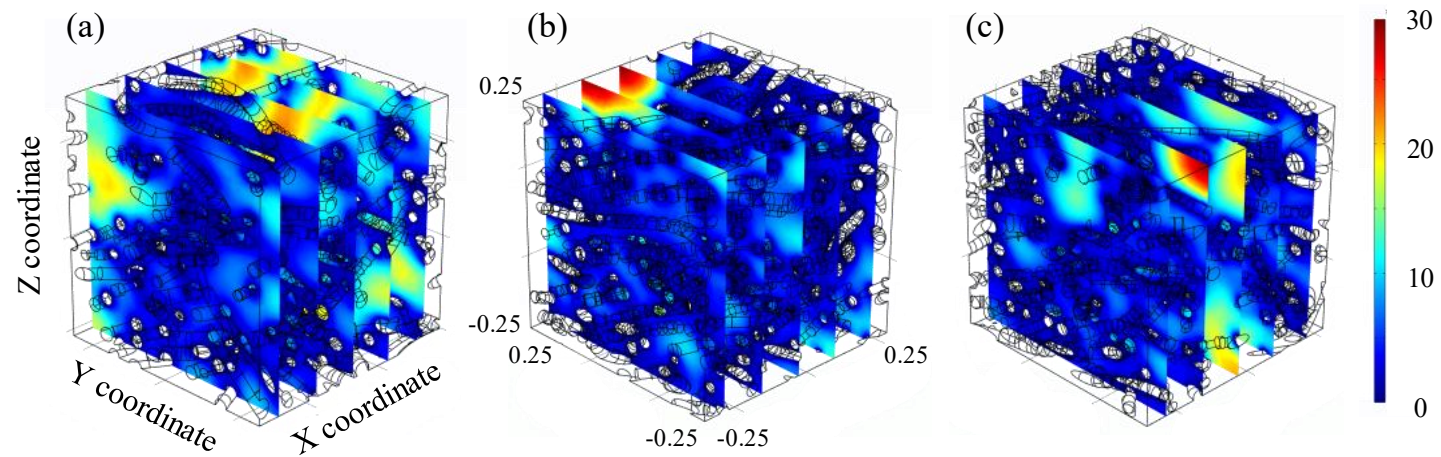


Figure 4.18 Heat diffusion field (u) [$\times 10^{-10}\text{m}^2$] of the testing PETs. (a) PET A #3, (b) PET B #1 and (c) PET C #2.

CHAPTER 5

NEURAL NETWORK MODEL DEVELOPMENT FOR MULTI-LAYERED FIBROUS MATERIAL

5.1 Introduction

This chapter focuses on identifying the feasibility of an ANN model for estimating the sound absorption coefficient of multi-layered fibrous materials. While chapter 4 focused on the fibrous material itself, the method of estimating the absorption coefficient of multi-layered fibrous materials using ANN will be discussed in this chapter. The objective of this work is to accurately estimate the sound absorption coefficient of multi-layered fibrous material by using only one intrinsic parameter as an input variable. The result will be compared with the value obtained using the transfer matrix method (TMM).

The model configuration is briefly discussed in chapter 5.2, the theory of TMM is introduced in chapter 5.3. The validity of the developed ANN model is verified in chapter 5.4 for three different cases, finally, the limitation of the developed model is noted in chapter 5.5.

5.2 Materials and model development

In this chapter, four types of fibrous PET felt were used to train the ANN model. PET felt is commonly used on dash isolation pads or floor carpets in the form of multilayered structures. The neural network model was trained using the sound absorption coefficient of stacked PET felts composed of four layers. The four types of PET felt have different densities and static airflow resistivity values, which are listed in Table 5.1. The thickness of all fibrous felt used was between 5–10 mm, and each specimen was prepared by cutting the felt into samples with a circular cross-section with diameter of 29 mm. An example of a four-layered PET felt sample is shown in Fig. 5.1. Four specimens were prepared for each PET type, and each specimen was classified to be of the same type if the density and static airflow resistivity values fell within a certain range. Therefore, the static airflow resistivity of the PET felt prepared in four specimens by four types (16 specimens) was distributed over a wide range of 40000 to 220000 [Nsm^{-4}].

The data set consisted of 256 four-layered samples covering all possible multilayer structure combinations using the four types of PET. The sound absorption coefficient of all 256 samples was measured, and the boundaries between each layer were not bonded. The ANN model was trained using 230

samples out of the data set, which corresponded to about 90% of the 256 samples. Model performance was verified using the test set which consisted of the remaining 26 samples (combinations of 26 samples are shown in Fig. 5.2-4), the sound absorption coefficient of the test set is estimated and compared to measured values. The ANN architecture is shown in Fig. 5.5. The input layer was divided into four parts, and each part was configured to input the thickness, density, and static airflow resistivity of one felt layer. The output value is the sound absorption coefficient of the four-layered fibrous material, for 56 frequencies, at 100 Hz intervals in the range of 500 to 6000 Hz.

For the cost function, the MSE function of Eq. (4.2) was used. The ReLU function was used as the activation function of the artificial neurons, and the weights and biases of the network were optimized using the Adam algorithm. The initial values of the weights and biases were used as an initial “He” values [57] that are specific for the ReLU function. The gradient was calculated using back propagation. Finally, the mini-batch size was chosen to be 25 samples, and the implementation was carried out using PYTHON language. Fig. 5.6 shows the loss trend of the training and test set. As the training cycle is repeated, the weights and biases of the network are updated by the Adam algorithm reducing the error (loss) in Eq. (4.2). I observed that the loss is stable after about 2000 training cycles. At the end of 3000 training cycles, the MAPE between the

predicted and measured value of the sound absorption coefficient is 0.82%, showing high accuracy. Specific results and additional verification of the ANN model, using PET 5 and RESIN felt, are covered in chapter 5.4.

5.3 Conventional acoustical impedance models

5.3.1 Transfer matrix for layered fibrous material

Here, the TMM is used to describe acoustic fields before and after layered acoustical materials [37, 39, 58]. The general expression of the TMM is as follows:

$$\begin{aligned}\begin{Bmatrix} p \\ v_y \end{Bmatrix}_{x=0} &= [T_{Layer\ 1}][T_{Layer\ 2}] \cdots [T_{Layer\ n}] \begin{Bmatrix} p \\ v_y \end{Bmatrix}_{x=t} \\ &= [T_{total}] \begin{Bmatrix} p \\ v_y \end{Bmatrix}_{x=t} = \begin{bmatrix} T_{11} & T_{12} \\ T_{21} & T_{22} \end{bmatrix} \begin{Bmatrix} p \\ v_y \end{Bmatrix}_{x=t},\end{aligned}\tag{5.1}$$

where p is the acoustic pressure, v_y is the normal acoustic particle velocity, T is the transfer matrix of the arbitrary layer, and t is the total thickness of multilayer. Once the elements of the transfer matrix are obtained, all the acoustical properties, such as reflection, absorption, and transmission coefficients, can be calculated. Using the total transfer matrix of Eq. (5.1), the reflection coefficient: $R(\theta)$ and sound absorption coefficient: α of the layered material can be calculated by applying the below expressions:

$$R(\theta) = \frac{T_{11} - (\rho_0 c_0 / \cos \theta) T_{21}}{T_{11} + (\rho_0 c_0 / \cos \theta) T_{21}}, \quad (5.2)$$

and

$$\alpha = \int_0^{\theta_{lim}} (1 - |R(\theta)|^2) \sin \theta \cos \theta d\theta, \quad (5.3)$$

where $\rho_0 c_0$ is the characteristic impedance of air, ρ_0 is the density of air, c_0 is the velocity of sound, and θ is the incident angle of the sound waves.

The transfer matrix is well organized to describe materials such as fibrous material, and elastic porous material. In this study, we used the TMM to obtain the normal incidence sound absorption coefficient of layered fibrous materials to compare with the results of the ANN model developed in chapter 5.2. In the case of fibrous material, it can be considered a limp or rigid porous material [37, 39, 58], and the transfer matrix for limp or rigid porous material is as defined below:

$$[T_{Rigid,Limp}] = \begin{bmatrix} \cos kd & jZ_c \sin kd \\ j \sin kd / Z_c & \cos kd \end{bmatrix}, \quad (5.4)$$

where Z_c is the characteristic impedance of the acoustical material, k is the wave number in the acoustical material, and d is the thickness of a layer. Two models for obtaining these acoustical properties are discussed in chapter 5.3.2.

5.3.2 Empirical model and motionless skeleton model

Empirical models consist of several coefficients that correlate the impedance and wave number with static airflow resistivity. Empirical models are developed by applying regression using the measurements of these particular values. Delany and Bazely [3] have proposed simple empirical expressions with a power law relation for fibrous materials. The established method consists of two indices, Eq. (5.5) and Eq. (5.6), which represent the characteristic impedance and the wave number. These indices are predicted simply based on the static airflow resistivity of materials and given by the following expressions:

$$Z_c = \rho_0 c_0 \left[1 + 9.08 \left(10^3 \frac{f}{\sigma} \right)^{-0.75} - j 11.9 \left(10^3 \frac{f}{\sigma} \right)^{-0.73} \right], \quad (5.5)$$

and

$$k = \frac{\omega}{c_0} \left[1 + 10.8 \left(10^3 \frac{f}{\sigma} \right)^{-0.70} - j 10.3 \left(10^3 \frac{f}{\sigma} \right)^{-0.59} \right], \quad (5.6)$$

where f is the frequency, and σ is the static airflow resistivity. The characteristic impedance and wave number obtained through the Delany and Bazely model can be substituted into Eq. (5.4) to form a transfer matrix of fibrous material. Many subsequent empirical models have been proposed since the Delany and Bazely model, Miki [4] and Komatsu [59] have proposed modified models to predict the acoustical behavior of different materials. Empirical models are still widely used because of their simplicity: only the static airflow resistivity is needed to describe the acoustical behavior. However, it should be noted that each model is only valid for specific types of materials [6].

Motionless skeleton models start with the assumption that the skeleton of the porous media is rigid and motionless when its density and stiffness is much larger than that of air. From the work of Zwikker and Kosten [9], motionless skeleton materials can be considered analogous to cylindrical tubes when describing acoustic behavior. The acoustic wave equation in the tube is given by the following equation:

$$\nabla^2 p + \frac{\rho_{eq}}{K_{eq}} p = 0, \quad (5.7)$$

where ρ_{eq} represents the complex bulk density, which can describe the effect of viscous resistance and K_{eq} is the complex bulk modulus, which describes the effect of thermal conduction. These two variables can be described by a given pore shape inside the porous media. Johnson, Champoux, and Allard [7, 8] proposed the complex bulk density and modulus of acoustical material, with a motionless skeleton having arbitrary pore shapes given by Eqs. (5.8) to (5.11), and several intrinsic parameters are considered during the modeling procedure. The arbitrary pore shapes are described by

$$\rho_{eq} = \alpha_\infty \rho_0 \left[1 + \frac{\sigma \phi}{j \omega \rho_0 \alpha_\infty} G_{J1}(\omega) \right], \quad (5.8)$$

$$G_{J1}(\omega) = \sqrt{1 + j \frac{4 \alpha_\infty^2 \eta \rho_0 \omega}{\sigma^2 \Lambda^2 \phi^2}}, \quad (5.9)$$

$$K_{eq} = \gamma P_0 / \left[\gamma - (\gamma - 1) \left(1 + j \frac{\sigma \phi}{\omega \rho_0 P_\gamma \alpha_\infty} G_{J2}(P_\gamma \omega) \right)^{-1} \right], \quad (5.10)$$

and

$$G_{J2}(P_\gamma\omega) = \sqrt{1 + j \frac{\rho_0 \Lambda'^2 P_\gamma \omega}{16\eta}}, \quad (5.11)$$

where P_0 is the atmospheric pressure; ρ_0 is the density of air; γ is the specific heat ratio of air; P_γ is the Prandtl number of air, and η is the viscosity of air. Using the complex bulk density and modulus, Eq. (5.8) and Eq. (5.10) respectively, the characteristic impedance of the material can be calculated as $Z_c = \sqrt{\rho_{eq} K_{eq}}$, and the wave number can be calculated as $k = \omega \sqrt{\rho_{eq} / K_{eq}}$. The characteristic impedance and wave number obtained through the JCA model can be substituted into Eq. (5.4) to form a transfer matrix of fibrous material.

For ANN and Delany-Bazely models, only the static airflow resistivity (σ) is needed to predict the acoustic behavior of a layered fibrous material. However, the JCA model requires five intrinsic parameters. Intrinsic parameters were obtained in the same way as in chapter 3.3. The measured intrinsic parameters of fibrous materials used in this study, excluding static airflow resistivity are shown in Table 5.2.

5.4 Model validation

In this chapter, the accuracy of the sound absorption coefficient prediction model using ANN and TMM is investigated. The required characteristic impedance and wave number for the transfer matrix are obtained by both the empirical model (the Delany-Bazely model) and the motionless skeleton model (the JCA model). The case where the transfer matrix is constructed using the Delany-Bazely model will be referred to as TMM-DB, and the case wherein the transfer matrix is constructed using the JCA model will be referred to as TMM-JCA. Note that the ANN and TMM-DB models require only one intrinsic parameter, σ , to estimate the sound absorption coefficient. In the case of TMM-JCA, five intrinsic parameters, σ , α_∞ , ϕ , Λ , and Λ' , are needed.

As mentioned in chapter 5.2, the ANN model is trained using 230 samples of PET felts stacked in four layers. To verify the generality of the trained model, I divided the three cases and confirmed the accuracy of the ANN model. The first case deals with 26 samples of four-layered PET combinations consisting of the same materials. In the second case, 26 samples of four-layered PET combinations were used with at least one different PET layer (PET 5) from the first case. The 26 samples consist of 12 samples containing one layer of PET with a new density and static airflow resistivity, 10 samples containing two new

layers, 3 samples containing three new layers, and one sample having four new layers. Since the first layer has the highest contribution when determining the sound absorption coefficient of the layered materials, out of the 26 samples, new PET layer was inserted at the first layer for 12 samples. The last case also deals with 26 samples of four-layered fibrous felt combinations with at least one RESIN felt layer in the PET combination of the first case. The composition of the combination with the RESIN felt is the same as in case 2. All detailed combinations of Case 1, 2, 3 are described in Fig. 5.2-4. For these three cases, the MAPE was obtained over the frequency range of 500–6000 Hz between the predicted absorption coefficient from the ANN, TMM, and the actual measurements for each of the 26 samples.

However, the four-layered samples covered in this study have a resonance phenomenon between 1500 and 3000 Hz. Dahl et al. [60] and Allard et al. [61] derived models that predict the sound absorption coefficient by dividing the frequencies at resonance and frequencies away from resonance. In the resonance frequency region, fiber motion should be considered, but another region shows motionless behavior. Since both TMM-DB and TMM-JCA models assume the motionless fiber skeleton, when comparing the MAPE of the ANN model and the TMM, only the frequency range of 3000-6000 Hz was considered. Then the difference between the predicted and measured values was

compared of the 26 samples at 4000 Hz.

5.4.1 Case no.1

In case 1, 26 samples were randomly selected from 256 four-layered PET felts to test the ANN model. The error of each sample was calculated, and the MAPE is shown in Fig. 5.7 in intervals of 100 Hz. The estimated sound absorption coefficient using TMM-DB shows an average error of 6.84% within the frequency range of 3000–6000 Hz. TMM-JCA shows an average error of 3.83%. When estimating the sound absorption coefficient using the ANN, the average error is 0.72%. The estimated sound absorption coefficient using the ANN of one randomly selected sample (sample 10 in Fig. 5.2) is shown in Fig. 5.8. It can be seen that the result fits very well with the measured sound absorption coefficient in the frequency range of interest. It is important to note that the four-layered PET causes resonance near 2500 Hz. This phenomenon is expected when high-density fibrous materials are stacked under an un-bonded condition in a normal direction to the incidence wave [60]. Although this is not a focus of this study, the trained ANN can predict the resonant frequency of the four-layered PET. The result at a single frequency of 4000 Hz is shown in Fig. 5.9. The black diagonal line represents a perfect correlation between the

predicted and the measured values. The average error was 7.18% for TMM-DB, 3.74% for TMM-JCA, and 0.38% for the ANN at 4000 Hz.

5.4.2 Case no.2

In Case 2, at least one new PET felt (*PET 5* from Table 5.1) that was not used when training the ANN was included in the four layers. The MAPE of each sample is shown in Fig. 5.10. TMM-DB shows an average error of 4.54% within the frequency range of 3000–6000 Hz, and TMM-JCA shows an average error of 2.46%. When using the ANN, the average error is 1.67%. Although the mean error is slightly higher than that of Case 1, it still shows consistent results. Out of the 26 samples in Case 2, the sample consisting of four layers of new PET is expected to be the most difficult to predict (sample 18 in Fig. 5.3). The estimated sound absorption coefficient, using the ANN of that sample, shown in Fig. 5.11 with measured values. However, the measured and estimated values show good correlation, suggesting that the developed ANN can accurately estimate the sound absorption coefficient of a four-layered structure composed of new PET of the same series. The result at a single frequency of 4000 Hz is shown in Fig. 5.12. An average error of 3.75% was observed with TMM-DB, 1.64% with TMM-JCA, and 1.30% with ANN at 4000 Hz.

5.4.3 Case no.3

In Case 3, at least one RESIN felt is included in four layers as described as *RESIN* from Table 5.1. Cases 1 and 2 deal with same series of PET, but in Case 3, the generality of the ANN model is examined using RESIN felt. The MAPE of each sample is shown in Fig. 5.13. TMM-DB shows an average error of 5.20% within the frequency range of 3000–6000 Hz, and TMM-JCA shows an average error of 3.10%. For the ANN, the average error is 1.25%. Again, the average error is slightly higher than Case 1, but with better accuracy than the estimated values of TMM. As with Case 2, the sample consisting of four layers of RESIN is expected to be the most difficult to predict out of the 26 samples in Case 3 (sample 18 in Fig. 5.4). The estimated sound absorption coefficient, using the ANN of that sample, is shown in Fig. 5.14. As with the four-layered PET, resonance occurs, but the region of the resonance frequency changes as the material of the skeleton is changed from PET to RESIN. For reference, micro computed tomography images of the two felt types are included in Fig. 5.15 to visually identify the structural differences between the RESIN and PET felts. Since the ANN model is trained based on the PET skeleton, it is assumed that the sample consists of a PET skeleton with the airflow resistivity of RESIN felt. Except for the region where resonance occurs, the remaining frequency

range shows an accurate estimated value. Although it is impossible to predict the resonance frequency of samples made of different materials with the ANN model, I can confirm that the model works well when only the fluid medium property is considered. The result at a single frequency of 4000 Hz is shown in Fig. 5.16. An average error of 3.75% is observed with TMM-DB, 1.64% with TMM-JCA, and 1.30% with ANN at 4000 Hz.

5.5 Limitations of the model

The result shows a positive starting point for multi-layered acoustical material research, neural network models that require more input variables might be needed for future work. Since the model was trained only with PET felt, a database containing a wider range of data is required to expand the range of acoustical materials to which this model can be applied. Additionally, it is important to point out that the model developed in this paper was trained only using data set for layers under the un-bonded boundary condition. Further research will focus on collecting more data from specimens with different fiber skeletons and a wider range of thickness and airflow resistivity values. By enlarging the database, it is possible to estimate the acoustic performance of multilayered acoustical materials for a wider variety of materials and layers. This allows the accurate estimation of acoustic performance while reducing the time and effort required for measuring intrinsic parameters. Furthermore, it is also possible to design the neural network model that covers the characteristics of the bonded boundary condition, because it is often difficult to predict the accurate performance of bonded multilayered acoustical materials using the TMM.

TABLE 5.1 Properties of PET and RESIN felts.

Specimen Name	<i>used to train & test the ANN model</i>				<i>used only to test the ANN model</i>	
	<i>PET 1</i>	<i>PET 2</i>	<i>PET 3</i>	<i>PET 4</i>	<i>PET 5</i>	<i>RESIN</i>
Areal Density [GSM]	600±50	800±50	1200±50	1400±50	1000±50	1000±50
Airflow Resistivity [× 10 ³ Nsm ⁻⁴]	40–46	63–70	120–140	190–220	92–104	130–160

TABLE 5.2 Intrinsic parameters of PET and RESIN felts.

	Tortuosity (α_∞)	Porosity (ϕ)	VCL (Λ)	TCL (Λ')
<i>PET 1</i>	1.15±0.09	0.91±0.05	46.22±2.11	111.58±7.20
<i>PET 2</i>	1.04±0.10	0.86±0.05	30.33±3.10	106.78±8.91
<i>PET 3</i>	1.14±0.12	0.82±0.05	22.90±1.89	139.06±6.18
<i>PET 4</i>	1.10±0.11	0.78±0.05	15.75±0.74	150.77±3.21
<i>PET 5</i>	1.09±0.12	0.84±0.05	24.19±1.72	117.72±4.21
<i>RESIN</i>	1.03±0.08	0.87±0.04	20.70±1.26	70.56±2.04



Figure 5.1 Example of a four-layered PET sample with a circular cross-section.

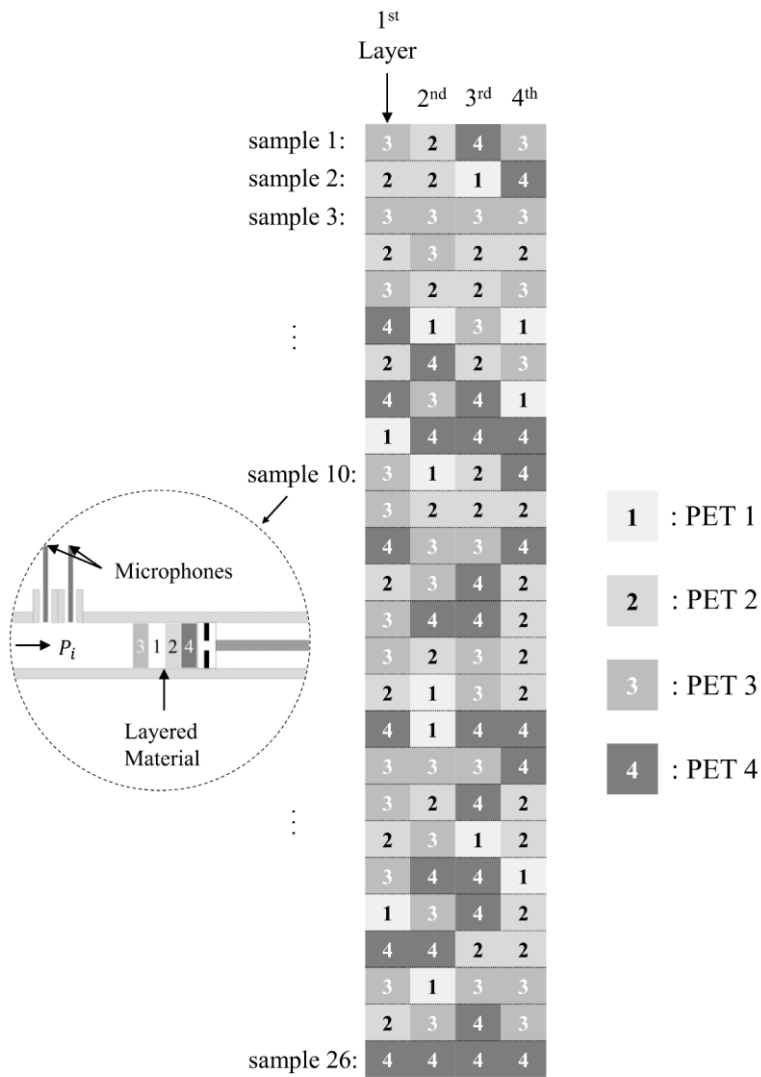


Figure 5.2 26 four-layered fibrous felt samples used in Case no.1.

	1 st Layer	2 nd	3 rd	4 th
sample 1:	1	1	1	5 ^N
sample 2:	1	2	5 ^N	5 ^N
sample 3:	1	5 ^N	1	1
	1	5 ^N	2	4
	1	5 ^N	4	5 ^N
⋮	1	5 ^N	5 ^N	4
	2	1	5 ^N	4
	2	2	5 ^N	5 ^N
	2	5 ^N	2	2
	2	5 ^N	4	1
	5 ^N	1	1	2
	5 ^N	1	1	4
	5 ^N	1	5 ^N	5 ^N
	5 ^N	2	1	2
	5 ^N	2	5 ^N	1
	5 ^N	2	4	4
	5 ^N	5 ^N	2	5 ^N
sample 18:	5 ^N	5 ^N	5 ^N	5 ^N
	5 ^N	5 ^N	4	5 ^N
	5 ^N	4	2	1
	5 ^N	4	5 ^N	1
⋮	5 ^N	4	5 ^N	4
	4	2	5 ^N	1
	4	5 ^N	1	5 ^N
	4	5 ^N	5 ^N	2
sample 26:	4	4	5 ^N	5 ^N

5^N : PET 5 (New PET)

Figure 5.3 26 four-layered fibrous felt samples used in Case no.2.

	1 st Layer	2 nd	3 rd	4 th
sample 1:	1	1	1	R
sample 2:	1	2	R	R
sample 3:	1	R	1	1
	1	R	2	4
	1	R	4	R
⋮	1	R	R	4
	2	1	R	4
	2	2	R	R
	2	R	2	2
	2	R	4	1
	R	1	1	2
	R	1	1	4
	R	1	R	R
	R	2	1	2
	R	2	R	1
	R	2	4	4
	R	R	2	R
sample 18:	R	R	R	R
	R	R	4	R
	R	4	2	1
	R	4	R	1
⋮	R	4	R	4
	4	2	R	1
	4	R	1	R
	4	R	R	2
sample 26:	4	4	R	R

R : RESIN

Figure 5.4 26 four-layered fibrous felt samples used in Case no.3.

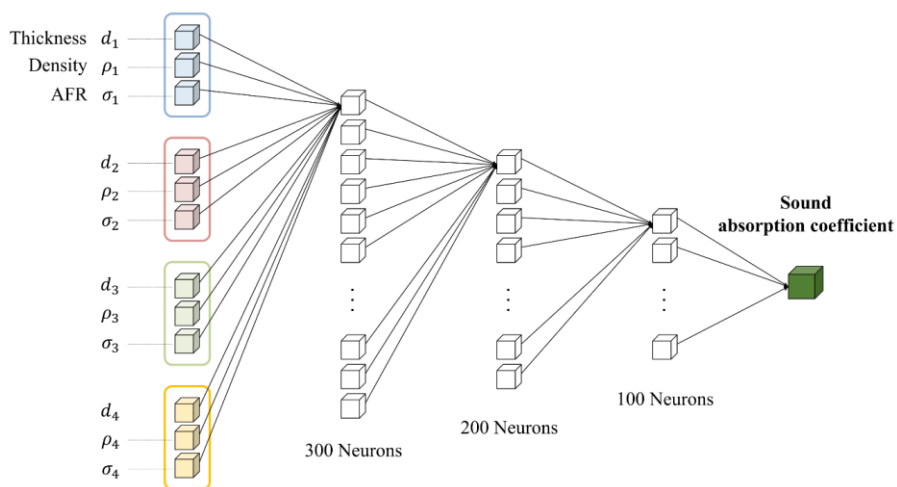


Figure 5.5 Structure of the ANN developed for estimating the sound absorption coefficient of a layered fibrous material.

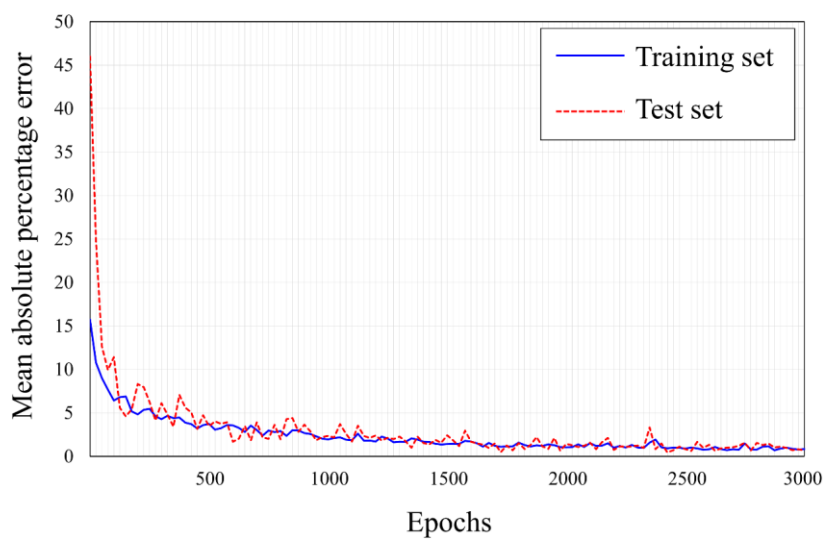


Figure 5.6 Trend of loss (percentage error) versus the number of training iterations (epochs).

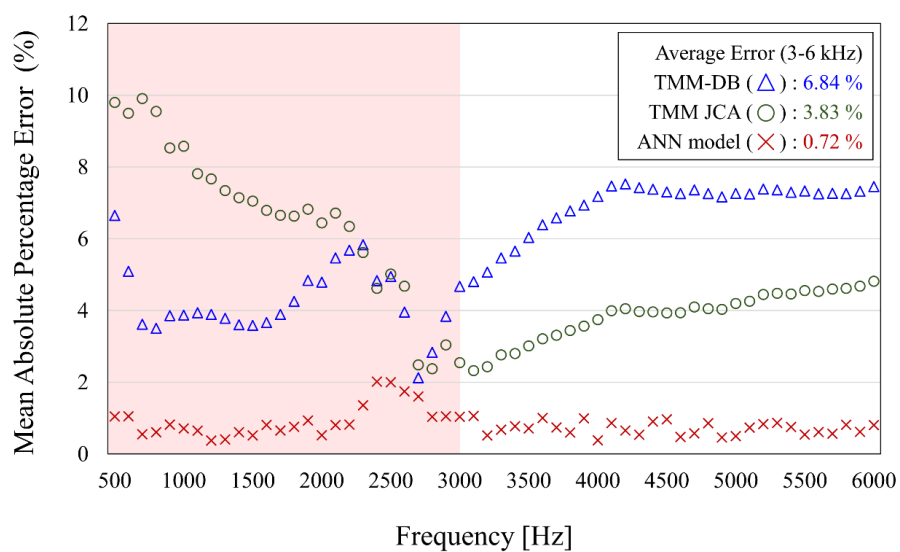


Figure 5.7 MAPE of estimated sound absorption coefficient using the

TMM-DB (△), TMM-JCA (○), and ANN model (×) for Case 1.

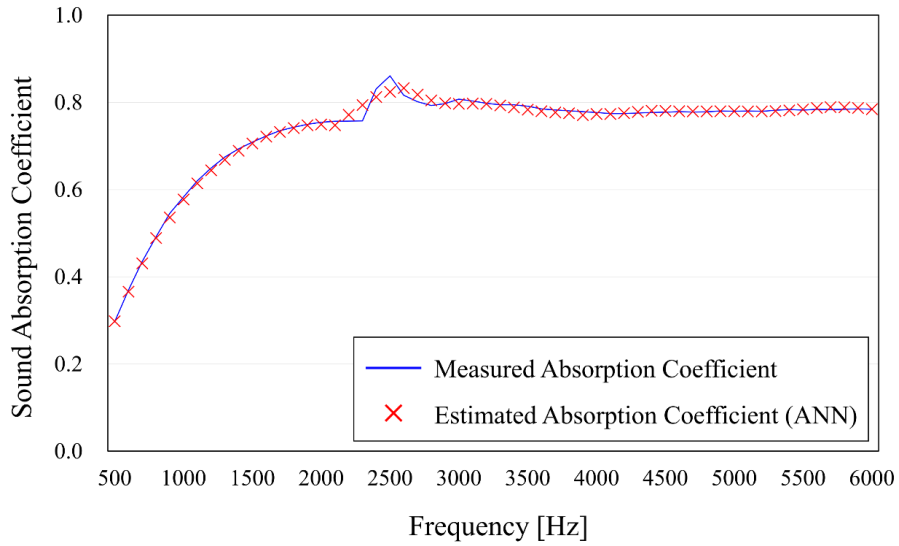


Figure 5.8 Estimated sound absorption coefficient using an ANN for one randomly selected sample out of 26 samples for Case 1. (sample 10 in Fig. 5.2)

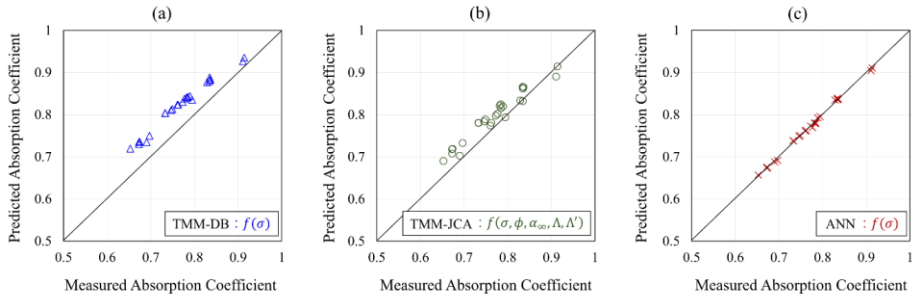


Figure 5.9 Estimated sound absorption coefficient of 26 samples at 4000 Hz using (a) TMM-DB, (b) TMM-JCA, and (c) ANN model for Case 1.

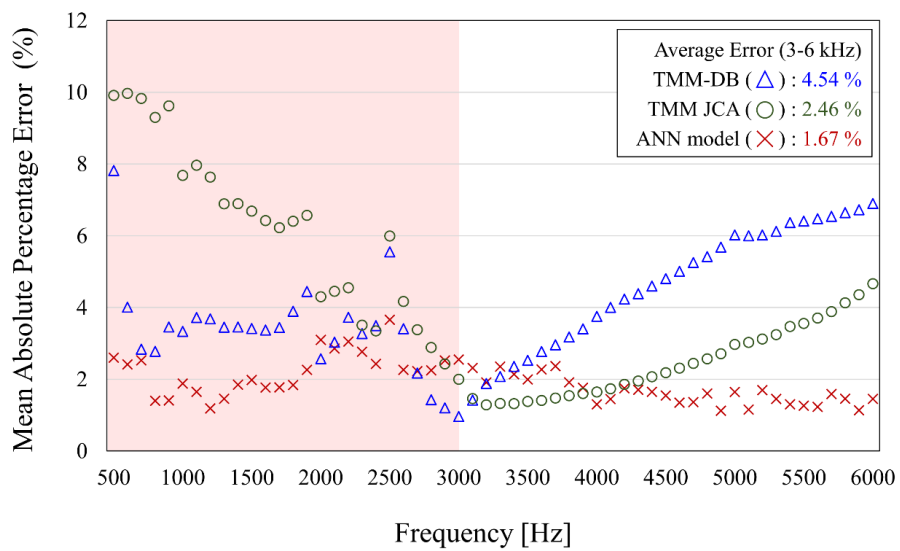


Figure 5.10 MAPE of estimated sound absorption coefficient using the TMM-DB (△), TMM-JCA (○), and ANN model (×) for Case 2.

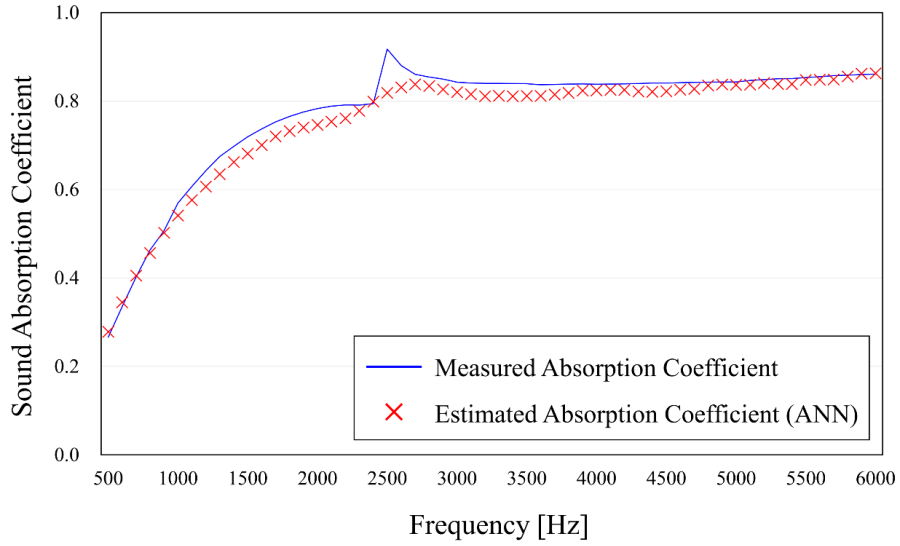


Figure 5.11 Estimated sound absorption coefficient using an ANN for Case 2, wherein the sample consisted of four layers of new PET. (sample 18 in Fig 5.3)

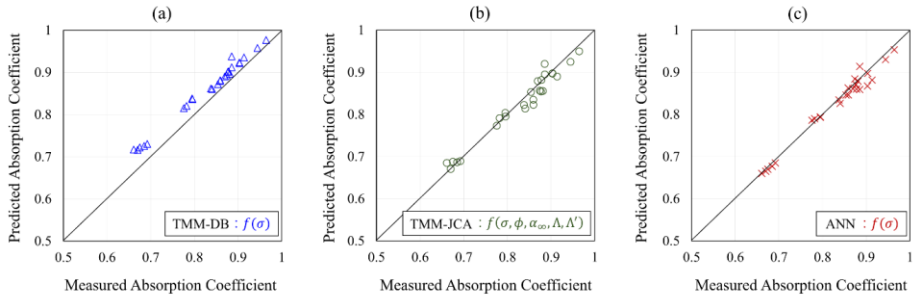


Figure 5.12 Estimated sound absorption coefficient of 26 samples at 4000 Hz using (a) TMM-DB, (b) TMM-JCA, and (c) ANN model for Case 2.

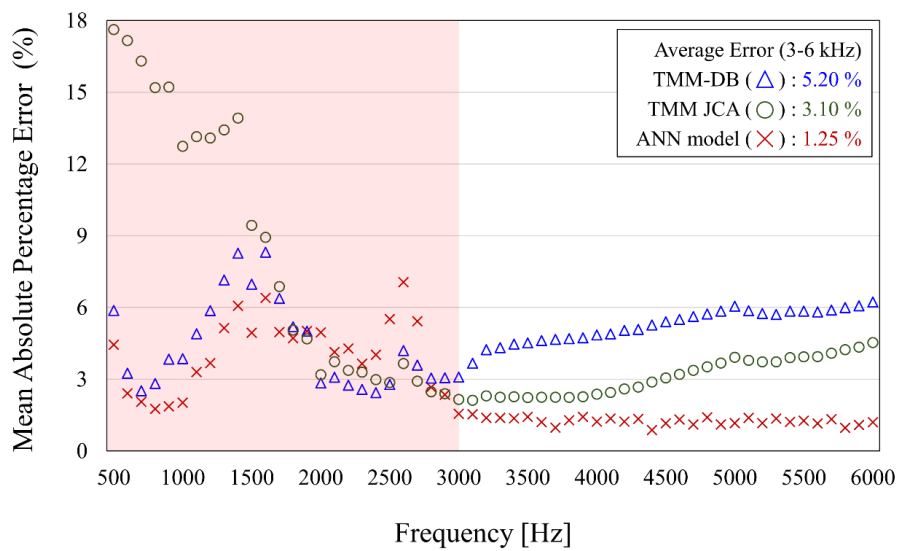


Figure 5.13 MAPE of estimated sound absorption coefficient using the TMM-DB (\triangle), TMM-JCA (\circ), and ANN model (\times) for Case 3.

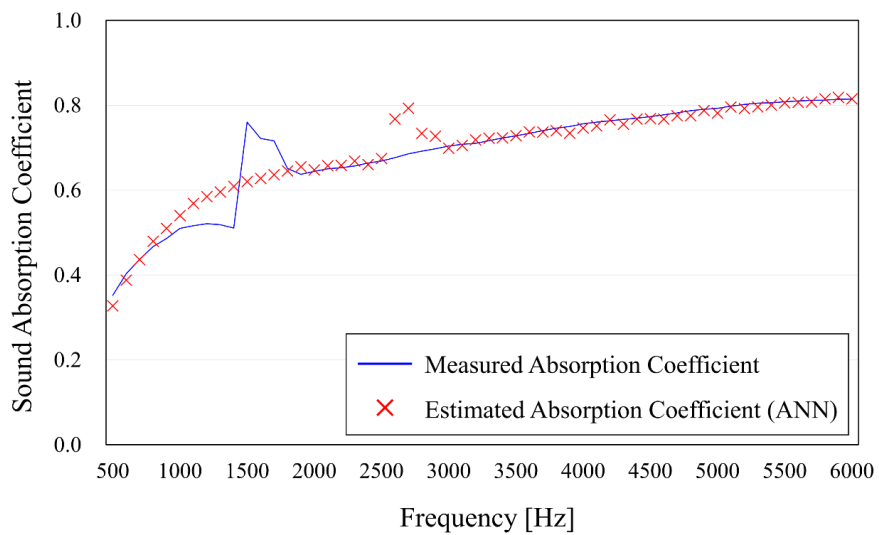


Figure 5.14 Estimated sound absorption coefficient using an ANN for Case 3, wherein the sample consisted of four layers of RESIN. (sample 18 in Fig 5.4)

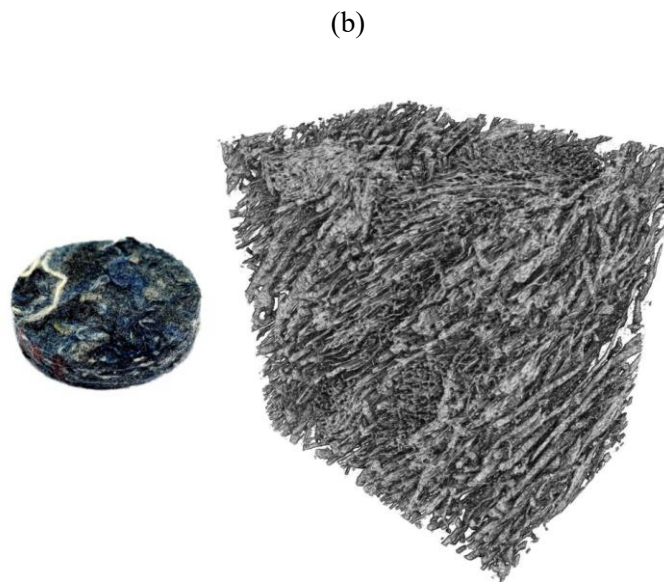
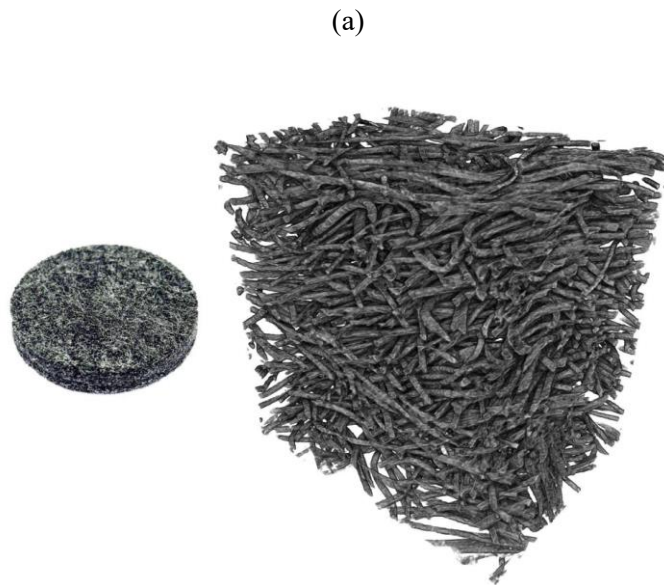


Figure 5.15 Micro computed tomography images of (a) PET and (b) RESIN felt. ($2800 \times 2800 \times 1950$ voxels with a resolution of $0.95 \mu\text{m}/\text{voxel}$)

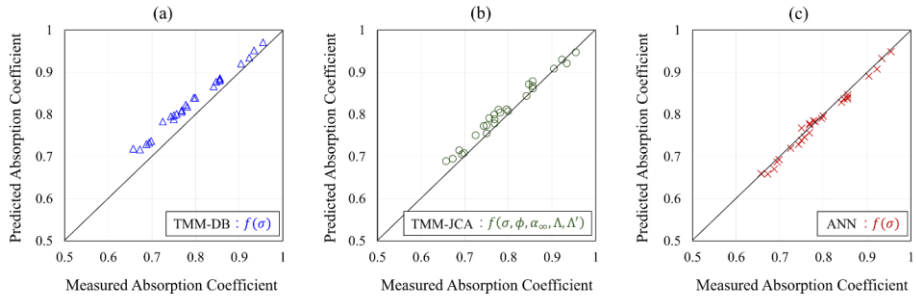


Figure 5.16 Estimated sound absorption coefficient of 26 samples at 4000 Hz

using (a) TMM-DB, (b) TMM-JCA, and (c) ANN model for Case 3.

CHAPTER 6

CONCLUSION

In this study, a method for predicting intrinsic parameters of fibrous materials using micro-CT images and CNNs and an ANN model for predicting the acoustical property of multi-layered fibrous material were proposed. In the first phase of the study, micro-CT image was used to develop the CNN models. The 2-D geometry of the fibers distributed in the image was characterized using the DB-SCAN algorithm to obtain the intrinsic parameters from the micro-CT images. Numerical analysis was performed using 2-D geometrical models characterized from the micro-CT image to calculate the five intrinsic parameters. Of the five intrinsic parameters, porosity and TCL were obtained directly using a 2-D geometrical model, tortuosity and VCL were obtained from the result of potential flow analysis, and static airflow resistivity was obtained from the result of Stokes flow analysis. Six CNN models were developed using 2-D slice images and intrinsic parameters corresponding to the images. After the CNN models were trained using this data, a test dataset containing 2-D CT images of different fibrous materials was used to validate the CNNs. The prediction accuracy of the developed CNN models was evaluated by comparing

the predicted intrinsic parameters of the fibrous volume with the values measured using traditional methods. The measured and predicted values showed good correlation. From the results, it was concluded that it is possible to predict the intrinsic parameters of fibrous material through CNNs using only 2-D micro-CT images, under limited range of orientation angle.

In the second phase of the study, the feasibility of a data-based ANN for the estimation of the sound absorption coefficient of multi-layered fibrous material is studied. The results demonstrate that it is possible to estimate the sound absorption coefficient of multilayered acoustical material using a neural network. Specifically, the sound absorption coefficient of four-layered fibrous material, in the frequency range of 500 to 6000 Hz, is estimated by a well-trained ANN that is based on the thickness, density, airflow resistivity, and sequence of the fibrous materials. For the three cases studied in this paper, the neural network model uses one intrinsic parameter and shows better estimation accuracy than the TMM using one or five parameters, especially in the high-frequency range. Note that these results were validated for the types of material, range of airflow resistivity, the density, and the thickness of materials used in this work.

This study dealt with methods to obtain physical quantities more simply and quickly by applying artificial intelligence to the field of acoustical materials.

The strength of artificial intelligence in terms of predicting physical quantities is that once the model is constructed, results can be derived through a set of input variable without in-depth of knowledge in the relevant field. Since acoustical materials are very important in the field of sound design, artificial intelligence can be an efficient tool for the needs of predicting the performance of acoustical materials without background knowledge in this field. As many engineers in the field of acoustical materials are making great efforts to graft artificial intelligence into this field, I look forward to meeting creative and surprising technologies in the near future.

REFERENCES

- [1] H. Shin and J. S. Bolton, “The identification of minimum-weight sound packages,” *Noise Control Eng. J.* 66, 523-540 (2018).
- [2] Y. Na and G. Cho, “Sound absorption and viscoelastic property of acoustical automotive nonwovens and their plasma treatment,” *Fiber. Polym.* 11, 782-789 (2010).
- [3] M. E. Delany and E. N. Bazley, “Acoustical properties of fibrous absorbent materials,” *Appl. Acoust.* 3, 105–116 (1970).
- [4] Y. Miki, “Acoustical properties of porous materials - Modifications of Delany-Bazely models,” *J. Acoust. Soc. Jpn.* 11, 19–24 (1990).
- [5] X. Tang and X. Yan, “Acoustic energy absorption properties of fibrous materials: A review,” *Compos. Part A Appl. Sci. Manuf.* 101, 360–380 (2017).
- [6] D. Oliva and V. Hongisto, “Sound absorption of porous materials – Accuracy of prediction methods,” *Appl. Acoust.* 74, 1473–1479 (2013).
- [7] D. L. Johnson, J. Koplik, and R. Dashen, “Theory of dynamic permeability and tortuosity in fluid-saturated porous media,” *J. Fluid Mech.* 176, 379–402 (1987).
- [8] Y. Champoux and J. F. Allard, “Dynamic tortuosity and bulk modulus in air-saturated porous media,” *J. Appl. Phys.* 70, 1975–1979 (1991).
- [9] C. Zwikker and C. W. Kosten, *Sound Absorbing Materials* (Elsevier, New York, 1949).

- [10] D. Lafarge, P. Lemarinier, J. F. Allard, and V. Tarnow, “Dynamic compressibility of air in porous structures at audible frequencies,” *J. Acoust. Soc. Am.* 102, 1995–2006 (1997).
- [11] S. R. Pride, F. D. Morgan, and A. F. Gangi, “Drag forces of porous-medium acoustics,” *Phys. Rev. B* 47, 4964–4978 (1993).
- [12] ISO 9053-1:2018(E) Acoustics – Determination of Airflow Resistance – Part 1: Static Airflow Method (International Standards Organization, Geneva, 2018).
- [13] A. Moussatov, C. Ayrault, and B. Castagnède, “Porous material characterization – Ultrasonic method for estimation of tortuosity and characteristic length using a barometric chamber,” *Ultrasonics*. 39, 195–202 (2001).
- [14] J. F. Allard, B. Castagnede, M. Henry, and W. Lauriks “Evaluation of tortuosity in acoustic porous materials saturated by air,” *Rev. Sci. Instrum.* 65, 754–755 (1994).
- [15] Y. Champoux, M. R. Stinson, and G. A. Daigle, “Air-based system for the measurement of porosity,” *J. Acoust. Soc. Am.* 89, 910–916 (1991).
- [16] Y. Salissou and R. Panneton, “Pressure/mass method to measure open porosity of porous solids,” *J. Appl. Phys.* 101, 124913 (2007).
- [17] V. Tarnow, “Airflow resistivity of models of fibrous acoustic materials,” *J. Acoust. Soc. Am.* 100, 3706–3713 (1996).
- [18] V. Tarnow, “Measured anisotropic airflow resistivity and sound attenuation of glass wool,” *J. Acoust. Soc. Am.* 111, 2735–2739 (2002).

- [19] K. Hirosawa and H. Nakagawa, “Formulae for predicting non-acoustical parameters of deformed fibrous porous materials,” *J. Acoust. Soc. Am.* 141, 4301–4313 (2017).
- [20] C. Perrot, R. Panneton, and X. Olny, “Periodic unit cell reconstruction of porous media: Application to open-cell aluminum foams,” *J. Appl. Phys.* 101, 113538 (2007).
- [21] C. Perrot, F. Chevillotte, and R. Panneton, “Dynamic viscous permeability of an open-cell aluminum foam: Computations versus experiments,” *J. Appl. Phys.* 103, 024909 (2008).
- [22] C. Perrot, F. Chevillotte, M. T. Hoang, G. Bonnet, F.-X. Bécot, L. Gautron, and A. Duval, “Microstructure, transport, and acoustic properties of open-cell foam samples: Experiments and three-dimensional numerical simulations,” *J. Appl. Phys.* 111, 014911 (2012).
- [23] J. H. Park, K. S. Minn, H. R. Lee, S. H. Yang, C. B. Yu, S. Y. Pak, C. S. Oh, Y. S. Song, Y. J. Kang, and J. R. Youn, “Cell openness manipulation of low density polyurethane foam for efficient sound absorption,” *J. Sound Vib.* 406, 224–236 (2017).
- [24] J. H. Park, S. H. Yang, H. R. Lee, C. B. Yu, S. Y. Pak, C. S. Oh, Y. J. Kang, and J. R. Youn, “Optimization of low frequency sound absorption by cell size control and multiscale poroacoustics modeling,” *J. Sound Vib.* 397, 17–30 (2017).
- [25] H. T. Luu, C. Perrot, V. Monchiet, and R. Panneton, “Three-dimensional reconstruction of a random fibrous medium: Geometry, transport, and sound absorbing properties,” *J. Acoust. Soc. Am.* 141, 4768–4780 (2017).

- [26] H. T. Luu, C. Perrot, and R. Panneton, “Influence of porosity, fiber radius, and fiber orientation on anisotropic transport properties of random fiber structures,” *Acta. Acust. united Ac.* 103, 1050–1063 (2017).
- [27] R. Lieblappen, J. M. Fegyveresi, Z. Courville, and D. G. Albert, “Using ultrasonic waves to determine the microstructure of snow,” *Front. Earth. Sci.* 8, 1-11 (2020).
- [28] H. R. Lee, S. S. Yang, J. W. Lee, and Y. J. Kang, “Estimation and uncertainty analysis of fluid-acoustic parameters of porous materials using microstructural properties,” *J. Acoust. Soc. Am.* 148, 308–323 (2020).
- [29] T. Lähivaara, L. Kärkkäinen, J. M. J. Huttunen, and J. S. Hesthaven, “Deep convolutional neural networks for estimating porous material parameters with ultrasound tomography,” *J. Acoust. Soc. Am.* 143, 1148–1158 (2018).
- [30] T. J. Chung, *Finite Element Analysis in Fluid Dynamics* (McGraw-Hill, New York, 1978).
- [31] J. Donea and A. Huerta, *Finite Element Methods for Flow Problems* (John Wiley and Sons, London, 2003).
- [32] D. Lesnic, L. Elliott, and D. B. Ingham, “Boundary element methods for determining the fluid velocity in potential flow,” *Eng. Anal. Bound. Elem.* 11, 203–213 (1993).
- [33] K. Sato, “Complex variable boundary element method for potential flow with thin objects,” *Comput. Methods Appl. Mech. Eng.* 11, 203–213 (1993).

- [34] M. Mokry, “Complex variable boundary element method for external potential flows,” *AIAA J.* 29, 207–208 (1991).
- [35] Y. Lecun, Y. Bengio, and G. Hinton, “Deep learning,” *Nature* 521, 436–444 (2015).
- [36] Y. Bengio, “Learning deep architectures for AI,” *Found. Trends Mach. Learn.* 2, 1–127 (2009).
- [37] J. F. Allard, N. Atalla, *Propagation of sound in porous media: modelling sound absorbing materials 2e*, (John Wiley and Sons, 2009).
- [38] J. S. Bolton, N. M. Shiau, Y. J. Kang, “Sound transmission through multi-panel structures lined with elastic porous materials,” *J. Sound Vib* (3) 317-347, (1996).
- [39] H. R. Lee, H. Y. Kim, J. H. Jeon, Y. J. Kang, “Application of global sensitivity analysis to statistical energy analysis: Vehicle model development and transmission path contribution,” *Appl. Acoust.* 146, 368-389, (2019).
- [40] R. Gooya, S. Bruns, D. Müter, A. Moaddel, R. P. Harti, S. L. S. Stipp, and H. O. Sørensen, “Effect of tomography resolution on the calculated microscopic properties of porous materials: Comparison of sandstone and carbonate rocks,” *Appl. Phys. Lett.* 109, 104102 (2016).
- [41] M. Ester, H-P. Kriegel, J. Sander, and X. Xu, “A density-based algorithm for discovering clusters in large spatial databases with noise,” In *Proceedings of 2nd International Conference on Knowledge Discovery and Data Mining* (AAAI Press, Menlo Park CA, 1996), pp. 226–231.

- [42] Y. Atalla and R. Panneton, "Inverse acoustical characterization of open cell porous media using impedance tube measurements," *Can. Acoust.* 33, 11–24 (2005).
- [43] ASTM E1050-98: Standard Test Method for Impedance and Absorption of Acoustical Materials Using a Tube, Two Microphones, and a Digital Frequency Analysis System (ASTM International, West Conshohocken, PA, 2006).
- [44] J. Y. Chung, D. A. Blaser, "Transfer function method of measuring in-duct acoustic properties. I. Theory," *J. Acoust. Soc. Am.* 68, 907-913 (1980).
- [45] J. Y. Chung, D. A. Blaser, "Transfer function method of measuring in-duct acoustic properties. II. Experiment," *J. Acoust. Soc. Am.* 68, 914-921 (1980).
- [46] B. H. Song, J. S. Bolton, "A transfer-matrix approach for estimating the characteristic impedance and wave numbers of limp and rigid porous materials," *J. Acoust. Soc. Am.* 107, 1131-1152 (2000).
- [47] Z. Wang, C. D., Massimo, M. T. Tham, A. J. Morris, "A procedure for determining the topology of multilayer feedforward neural networks," *Neural Netw.*, 7 (2), 291-300 (1994).
- [48] J. H. Jeon, S. S. Yang, and Y. J. Kang, "Estimation of sound absorption coefficient of layered fibrous material using artificial neural networks," *Appl. Acoust.* **169**, 107476 (2020).
- [49] F. Wang, Z. Chen, C. Wu, Y. Yang, "Prediction on sound insulation properties of ultrafine glass wool mats with artificial neural networks," *Appl. Acoust.*, 146, 164-171 (2019).

- [50] R. Hecht-Nielsen, “Theory of the backpropagation neural network,” In Proceedings of the International Joint Conference on Neural Networks (SOS Printing, San Diego, CA, 1989), pp. 593–606.
- [51] Y. LeCun, L. Bottou, Y. Bengio, P. Haffner, “Gradient-based learning applied to document recognition,” Proceedings of the IEEE, 86 (11), 2278-2324 (1998).
- [52] J. Duchi, E. Hazan, Y. Singer, “Adaptive subgradient methods for online learning and stochastic optimization,” J. Mach. Learn. Res., 12, 2121-2159 (2011).
- [53] D. P. Kingma, J. L. Ba, Adam: “A method for stochastic optimization,” ArXiv e-print, (2014).
- [54] N. Buduma, *Fundamentals of Deep Learning: Designing Next-Generation Machine Intelligence Algorithms* (O’Reilly Media, Sebastopol, CA, 2017).
- [55] A. Krizhevsky, I. Sutskever, and G. E. Hinton, “ImageNet classification with deep convolutional neural networks,” In *Advances in Neural Information Processing Systems 25*, edited by F. Pereira, C. J. C. Burges, L. Bottou, and K. Q. Weinberger (Curran Associates, New York, 2012), pp. 1097–1105.
- [56] T. G. Zielinski, R. Venegas, C. Perrot, M. Cervenka, F. Chevillotte, K. Attenborough, “Benchmarks for microstructure-based modelling of sound absorbing rigid-frame porous media,” J. Sound Vib. **483**, 115441 (2020).

- [57] K. he, X. Zhang, S. Ren, J. Sun, "Delving deep into rectifiers surpassing human level performance on ImageNet classification," ArXiv e-print, (2015).
- [58] J. S. Bolton, N. M. Shiau, Y. J. Kang, "Sound transmission through multi-panel structures lined with elastic porous materials," *J. Sound Vib.* (3), 317-347 (1996).
- [59] T. Komatsu, "Improvement of the Delany–Bazley and Miki models for fibrous sound-absorbing materials," *Acoust. Sci. Tech.* 29 (2), 121-129 (2008).
- [60] M. D. Dahl, E. J. Rice, D. E. Groesbeck, "Effects of fiber motion on the acoustic behavior of an anisotropic, flexible fibrous material," *J. Acoust. Soc. Am.*, 87, 54-66 (1990).
- [61] J. F. Allard, C. Depollier, P. Guignouard, P. Rebillard, Effect of a resonance of the frame on the surface impedance of glass wool of high density and stiffness, *J. Acoust. Soc. Am.*, 89, 999-1001 (1991).

국 문 초 록

본 연구에서는 인공지능을 활용하여 단층 섬유형 음향재료의 전송 매개변수와 음향 물성, 다층 섬유형 음향재료의 음향 물성을 예측하는 기법에 대해 소개한다. 본 연구의 첫 장에서는, 합성곱 신경망(Convolutional neural network)과 재료의 단층촬영 이미지를 이용하여 섬유형 재료의 전송 매개변수를 예측한다. 2차원의 단층촬영 이미지를 이용해 추출한 기하 모델을 이용한 유동해석으로 전송 매개변수를 구하고, 이미지와 전송 매개변수를 이용해 합성곱 신경망 모델을 구성하였다. 유동해석은 Stokes 유동과 Potential 유동을 이용해 수치해석적으로 수행되었다. 2차원의 이미지를 적층하여 3차원의 이미지를 구성하는 단층촬영 기법의 방법론에 착안하여, 각 2차원 이미지와 합성곱 신경망을 이용해 구한 전송 매개변수를 합성하여 3차원 섬유 재료의 매개변수를 구한다. 합성곱 신경망을 이용해 구한 섬유형 재료의 전송 매개변수는 측정을 통해 구한 값으로 검증하였고, 높은 정확성을 나타내었다. 마지막으로 예측한 전송 매개변수를 이용해 재료의 흡음률을 예측하고, 마찬가지로 측정 값과 비교 검증하였다. 본 장의 결과에서, 인공지능 기술과 단층촬영 이미지만으로 음향재료의 전송 매개변수를 구하는 것이 가능함을 확인하였다. 본 연구의 두 번째 장에서는, 인공지능을 활용하여 다층 구조 섬유 재

료의 음향 물성을 예측하는 기법에 대해 다루었다. 정적 유동저항계수 하나의 전송 매개변수를 입력하는 인공신경망을 이용하여 4층 구조의 섬유탄 재료의 흡음계수를 예측하는 모델을 개발하였고, 측정 값과 비교 및 검증한다. 인공신경망을 구성하기 위한 훈련 데이터로는 실험적으로 측정한 230개 4층 섬유탄재료의 흡음률을 이용하였다. 인공신경망의 범용성을 확인하기 위해 세 가지 케이스를 나누어 검증을 수행하였다. 이때 다층 음향재료의 음향 물성을 예측하는데 널리 사용되는 전달행렬법 (Transfer matrix method)의 예측값과, 관내법을 이용해 측정한 값을 통해 인공신경망의 성능을 검증하였고, 본 연구에서 정의된 시험편의 조건에서 인공신경망이 매우 우수한 예측 성능을 보임을 확인하였다.

주요어 : 인공지능, 합성곱 신경망, 전송 매개변수,
단층촬영 이미지, 수치해석, 흡음 계수, 섬유탄 재료,
다층 다공질 재료

학 번 : 2013-23086